Research Square

Preprints are preliminary reports that have not undergone peer review.
They should not be considered conclusive, used to inform clinical practice,
or referenced by the media as validated information.

Formulation and in vitro assessment of Rutin-loaded Chitosan/Guar Gum Nanoparticles for Targeting Ovarian Cancer cells

Jeganpandi Senthamarai Pandi
Kalasalingam Academy of Research and Education
Parasuraman Pavadai
Ramaiah Institute of Technology
Murugesan Sankaranarayanan
Birla Institute of Technology and Science, Pilani
Pavithra Velmurugan
Mahatma Gandhi Medical College and Research Institute
Veni Subramanyam
Mahatma Gandhi Medical College and Research Institute
Yuan-Pin Chang
National Sun Yat-sen University
Santhana Krishna Kumar A.
National Sun Yat-sen University
Selvaraj Kunjiappan
selvapharmabio@gmail.com

SRM Institute of Science and Technology

Research Article

Keywords: Rutin, ovarian cancer cells, chitosan, guar gum, cytotoxicity, nanoparticles

Posted Date: September 11th, 2026

DOI: https://doi.org/10.21203/rs.3.rs-10834579/v1

License: This work is licensed under a Creative Commons Attribution 4.0 International License.
Read Full License

Additional Declarations:
No competing interests reported.

Tables are available in the Supplementary Files section.

Formulation and *in vitro* assessment of Rutin-loaded Chitosan/Guar Gum Nanoparticles for Targeting Ovarian Cancer cells

Jeganpandi Senthamarai Pandi[1,2], Parasuraman Pavadai[3], Murugesan Sankaranarayanan[4], Pavithra Velmurugan[5], Veni Subramanyam[5], Yuan-Pin Chang[2,6,7]*, A. Santhana Krishna Kumar [2*], Selvaraj Kunjiappan[8, 9*]

[1]Department of Biotechnology, Kalasalingam Academy of Research and Education, Krishnankoil, 626126, Tamil Nadu, India

[2]Department of Chemistry, National Sun Yat-sen University, No. 70, Lien-hai Road, Gushan District, Kaohsiung City-80424, Taiwan.

[3]Department of Pharmaceutical Chemistry, Faculty of Pharmacy, M.S. Ramaiah University of Applied Sciences, Bengaluru, 560054 India

[4]Medicinal Chemistry Research Laboratory, Department of Pharmacy, Birla Institute of Technology and Science Pilani, Pilani, 333031, Rajasthan, India

[5]Mahatma Gandhi Medical Advanced Research Institute, Sri Balaji Vidyapeeth, Pondicherry, 607402, India

[6]Department of Medicinal and Applied Chemistry, Kaohsiung Medical University, No. 100, Shiquan 1st Rd., 807378, Kaohsiung, Taiwan

[7]Aerosol Science Research Center, National Sun Yat-sen University, No. 70 Lien-hai Road, 804201, Kaohsiung, Taiwan

[8]Center for Computational Biology, SRM Institute of Science and Technology, Tiruchirappalli Campus, Tiruchirappalli, Tamil Nadu 621105, India

[9]Center for Research, Trichy SRM Medical Hospital and Research Center, Tiruchirappalli Campus, Tiruchirappalli, Tamil Nadu 621105, India

*Address to Correspondence

Dr. Yuan-Pin Chang, Professor, Email: ypchang@mail.nsysu.edu.tw

A. Santhana Krishna Kumar, Assistant Professor. Email: santhanakumarbits@gmail.com

Dr. Selvaraj Kunjiappan, Associate Professor, Email: selvapharmabio@gmail.com

Abstract

Rutin (RTN) is a naturally occurring flavonoid glycoside with potent antioxidant and anticancer properties; however, its therapeutic application is limited by poor water solubility, low stability, and reduced bioavailability. This study developed rutin-loaded chitosan/guar gum nanoparticles (RTN-CS/GG-NPs) via ionic gelation to improve RTN delivery and enhance its anticancer activity against ovarian cancer cells (SKOV-3). Chitosan was used to prepare the nanoparticles, followed by guar gum coating to enhance stability. The formulated RTN-CS/GG-NPs were characterized for their physicochemical properties, encapsulation efficiency, drug-release behavior, and cytotoxicity. RTN-CS/GG-NPs exhibited a semi-crystalline structure, spherical morphology, a mean particle size of 42.76 nm, and a positive zeta potential of +57.6 mV. The NPs formulation achieved an encapsulation efficiency of 86.71 ± 1.35% (w/w) and a drug-loading capacity of 9.88 ± 0.74% (w/w). *In vitro* release studies demonstrated controlled drug release, with the highest release (83.27 ± 0.55%) observed at pH 5.8. Cytotoxicity analysis revealed that RTN-CS/GG-NPs significantly inhibited SKOV-3 cell growth compared with free RTN, with an IC_{50} of 23.60 µg/mL after 24 h of treatment. The nanoparticles also increased intracellular reactive oxygen species (ROS) production, mitochondrial membrane potential loss, and induced apoptosis, as confirmed by membrane blebbing and nuclear disintegration. These findings indicate that RTN-CS/GG-NPs enhance intracellular RTN delivery and effectively suppress the proliferation of ovarian cancer cells. The developed nanoparticle system shows promise as a targeted nanocarrier to improve the therapeutic efficacy of RTN in ovarian cancer.

Keywords: Rutin, ovarian cancer cells, chitosan, guar gum, cytotoxicity, nanoparticles

1. Introduction

Cancer is a major societal health problem and continues to be one of the leading causes of morbidity and mortality across the world [1]. Accounting for roughly 10 million deaths and over 20 million new diagnoses every year. According to the Global Cancer Observatory (GLOBACON) survey, 19.30 million new cases were reported worldwide in 2020. In India, 14,61,427 cancer cases in 2022, and one in nine people may develop cancer in their lifespan [2]. India ranks third after the People's Republic of China and the United States of America for cancer, and with an estimated 2.08 million new cases in 2040, reflecting a 57.5% rise from the previous year, according to GLOBACON. Cancer affects the Indian population demographically unevenly, with the age between 40 to 64 years accounting for the most cancer cases. Children aged 0–14 years also experience a notable cancer burden, accounting for approximately 4% of all cancer cases, with an estimated prevalence of 3% among males and 1.8% among females [3]. In general, cancer is a complex and multifaceted disease characterized by self-sufficient growth, unregulated cell proliferation, prolonged new blood vessel formation, immune evasion, resistance to apoptosis, and evasion of normal cell-cycle signals [4]. Consequently, these characteristics are driven by genetic and epigenetic anomalies, which make diagnosis and treatment challenging [5]. Moreover, approximately 90% of cancer-related deaths are caused by metastasis, where malignant cells spread uncontrollably or unregulated [6].

Among the various types of cancers, ovarian cancer is one of the most aggressive gynecological malignancies and predominantly affects older postmenopausal women [7]. It has a high mortality rate because it develops silently on the ovaries in the early stages, with late signs, less sensitivity and specificity of the screening, and leading to late detection at stage III or IV, where the metastatic malignancy has spread to other parts of the body, including the abdomen and pelvis [8]. According to the National Cancer Institute (NCI), an estimated 20,890

new cases of ovarian cancer and 12,730 ovarian cancer-related deaths were projected in 2025 [9]. Ovarian cancer comprises several histological subtypes, each characterized by distinct molecular alterations. These include low-grade endometrioid carcinoma (LGEC), commonly associated with PTEN, ARID1A, and PIK3CA mutations; high-grade serous carcinoma (HGSC), characterized by BRCA1/2 and TP53 mutations; low-grade serous carcinoma (LGSC), frequently associated with KRAS and BRAF mutations; clear cell carcinoma, commonly harboring ARID1A and PIK3CA mutations; and mucinous carcinoma, which is predominantly associated with KRAS mutations [10]. HGSC originates from the fallopian tube or peritoneum, and other subtypes, such as clear cell carcinoma and endometrioid carcinoma, originate from endometrial tissue [11]. Clinical signs and symptoms of ovarian cancer include continuous vomiting, abdominal pain and swelling, frequent urination, irregular bowel movements, lower back or pelvic pain, and appetite loss [12]. The incidence of ovarian cancer continues to increase worldwide due to a combination of genetic, hormonal, reproductive, lifestyle, and environmental risk factors. Older age, particularly among postmenopausal women, remains one of the significant risk factors. Inherited genetic predispositions, including pathogenic variants in BRCA1, BRCA2, and genes associated with Lynch syndrome, substantially increase the risk of developing ovarian cancer. Reproductive and hormonal factors, such as early menarche (before 12 years of age), late menopause (after 52 years), and prolonged exposure to estrogen, including postmenopausal hormone therapy, have also been implicated in disease development. In addition, modifiable lifestyle factors, including excessive alcohol consumption, unhealthy dietary patterns characterized by frequent intake of fast and processed foods, overweight and obesity, physical inactivity, tobacco use, cigarette smoking, inadequate sleep, and other unhealthy lifestyle behaviors, may contribute to an elevated risk. Furthermore, certain gynecological conditions, particularly endometriosis, are associated with an increased risk of specific ovarian cancer subtypes [13]. Currently, various

diagnostic techniques are utilized for ovarian cancer detection, including blood tests for cancer antigen 125 (CA-125), pelvic examination (including development or alterations of the uterus and ovaries), imaging modalities such as transvaginal ultrasound, magnetic resonance imaging (MRI) and CT scans, and biopsies [14]. Early diagnosis of ovarian cancer is associated with improved survival outcomes, whereas advanced-stage disease is often difficult to treat because of extensive metastasis and reduced therapeutic efficacy [15]. Various treatment strategies are followed to treat ovarian cancer, including hysterectomy (removal of the uterus, fallopian tubes, and ovaries), radiation therapy, chemotherapy (including platinum-based cytotoxic chemotherapy), targeted therapies (such as antiangiogenic agents, poly (ADP-ribose) polymerase (PARP) inhibitors, and anti-vascular endothelial growth factor (VEGF), hormone therapy, and immunotherapy [16]. Current therapeutic approaches, including chemotherapy, radiotherapy, and other systemic treatments, are often associated with significant limitations and adverse effects, such as reduced recovery rate, high toxicity, damage to healthy cells, multi-drug resistance, increased DNA damage, lengthy treatment durations, high cost of treatment, cancer recurrence, and non-specific targeting of cancer cells [17].

To overcome these issues, researchers are focusing on plant-derived compounds as a potential alternative to chemotherapy (chemically synthesized), because they are less toxic, more affordable, renewable, biocompatible, and effective against various cancer cell types [18, 19]. Bioactive compounds discovered in plants, including roots, flowers, leaves, seeds, fruits, and stems [20]. A variety of bioactive compounds were derived from plants to treat various diseases, commonly utilized medicinal compounds including alkaloids (like piperine from *Piper longum* and *Piper nigrum*), flavonoids (like quercetin, curcumin from the Indian spice turmeric, resveratrol from grapes, red wine, pines, etc.), terpenes (like thymoquinone from *Nigella sativa*), and rutin, genistein, and kaempferol. Rutin (RTN) (quercetin 3-rutinoside, molecular formula: $C_{27}H_{30}O_{16}$) is a flavonoid which is isolated from citrus fruits, apples,

buckwheat (*Fagopyrum esculentum Moench*), tea, wine, and onions [21]. Extensive research reports highlight RTN's potential pharmacological activities, including anticancer, anti-inflammatory, antimicrobial, antioxidant, antidiabetic, cardioprotective, neuroprotective, and anti-angiogenic activities [22]. Ghorbani et al. reported that rutin is used to treat diabetes mellitus, cardiovascular issues, and hyperlipidemia due to its alleged insulin-sensitizing and lipid-lowering properties [23]. Also, Wang et al. reported that rutin reduces the risk of cardiovascular effects by increasing nitric oxide production and inhibiting nucleotide-binding domain-like receptor 3 (NLRP3), which is involved in ROS generation, thereby improving endothelial function [24]. Similarly, rutin has been shown to address neurodegenerative disorders by regulating microglia and astrocyte activation, controlling protein penetration, and inducing apoptosis [25, 26]. Further, rutin has a variety of anticancer mechanisms, such as increasing reactive oxygen species (ROS), triggering caspase activity, preventing malignant growth, stopping the cell cycle, triggering apoptosis, preventing angiogenesis and inflammation, causing oxidative stress, and controlling cell signalling pathways like phosphatidylinositol 3-kinase (PI3K)/ protein kinase B (Akt/PKB), Mitogen-Activated Protein Kinase (MAPK), NF-κB (Nuclear Factor kappa B), and Vascular Endothelial Growth Factor (VEGF) [27]. At the same time, therapeutic applications of rutin are limited by poor water solubility and stability, which results in low bioavailability at the target site [28]. Researchers develop suitable nanoformulations to overcome this limitation to enhance the bioavailability at the target site. These nanoformulations can enhance delivery, reverse multidrug resistance, and release RTN directly to tumor sites [29]. Most studies demonstrated that nanoparticles (NPs) use passive targeting via the Enhanced Permeability and Retention (EPR) effect to improve targeting efficiency due to their high vascular permeability [30]. However, NPs have been encapsulated with hydrophobic or hydrophilic drugs, and commonly used nanoparticles include solid lipid NPs, liposomes, polymeric NPs, micelles, dendrimers, mesoporous silica

NPs, gold and silver NPs, and carbon nanotubes [31, 32]. Recently, polymeric NPs have been widely used for drug delivery because of their enhanced stability and bioavailability at the target site, high loading capacity, avoidance of premature degradation, controlled and pH-dependent release, and enhanced accumulation in tumour cells via the EPR effect [33].

Chitosan, a natural polymer derived from crustacean shells and insects, is widely used in drug delivery applications for its excellent biocompatibility, controlled release, resistance to enzymatic degradation, improved permeability, enhanced pharmacological effects, mucoadhesion, targeted delivery, and non-toxicity [34]. The polycationic characteristics of chitosan make it a promising nanocarrier for targeted cancer therapy. The protonated amino groups in chitosan facilitate electrostatic interactions with the negatively charged surfaces of cancer cells, thereby promoting enhanced cellular uptake via energy-dependent endocytic pathways. This efficient internalization enables the controlled delivery of therapeutic agents directly into tumor cells, improving drug localization and therapeutic efficacy [35]. When integrated with naturally derived guar gum, a galactomannan polysaccharide obtained from *Cyamopsis tetragonoloba*, chitosan-based nanoparticles exhibit improved physicochemical properties. The incorporation of guar gum enhances nanoparticle stability, biodegradability, and gel-forming ability while minimizing particle aggregation. Further, this combination improves drug encapsulation efficiency, maintains structural integrity, extends systemic circulation time, and facilitates sustained and controlled release of therapeutic agents [36]. Radwan et al. reported hepatoprotective effects of rutin-loaded chitosan/poly(acrylic acid) nanogels against hepatocellular carcinoma, upregulating Bax, caspases, and p53 while downregulating Bcl-2, inhibiting angiogenesis, and reducing hepatocellular carcinoma-related damage [37]. As a result, encapsulating RTN within biodegradable chitosan-guar gum nanoparticles may offer several benefits over existing drug delivery platforms. Therefore, this

study was designed to evaluate the cytotoxic potential of rutin-loaded chitosan/guar gum nanoparticles and assess their anticancer activity against SKOV3 human ovarian cancer cells.

2. Experimental section

2.1. Chemicals and cell line

Unless specified otherwise, all reagents utilized in this study were of purity ≥ 99 %. Rutin (chemical formula: $C_{27}H_{30}O_{16}$, and molecular weight (MW): 610.52 g/mol) was purchased from Sigma-Aldrich Pvt. Ltd., Bengaluru, India. Sodium alginate (chemical formula: $(C_6H_7NaO_6)_n$), chitosan (CS) (chemical formula: $(C_6H_{11}NO_4)_n$), and guar gum powder (GG) (GRM1233) were supplied by Himedia Laboratories Pvt Ltd., Mumbai, India. Sigma-Aldrich Private Limited, Bengaluru, India, provided Dulbecco's Modified Eagle's Medium (DMEM), fetal bovine serum (FBS), sodium tripolyphosphate, 1-ethyl-3-(3-dimethylaminopropyl) carbodiimide hydrochloride (EDAC), polyethylene glycol (NH_2–PEG–COOH), streptomycin, penicillin, and amphotericin B. Moreover, we purchased trypsin-EDTA solution, dimethyl sulfoxide (DMSO), 3-(4,5-dimethyl-2-thiazolyl)-2,5-diphenyl-tetrazolium bromide (MTT), dialysis membrane bags (MW: 3500 Da), phosphate buffer solutions (PBS), ethidium bromide (EB), acridine orange (AO), 4',6-diamidino-2-phenylindole (DAPI), rhodamine-123, and 2',7' dichlorofluorescin diacetate (DCFH-DA) from Gibco, New York, USA. The National Centre for Cell Science (NCCS) in Pune, India, supplied the fibroblast cells (L929 cells) and the SKOV-3 human ovarian cancer cell lines. Himedia Laboratories Private Limited, India, and Thermo Fisher Scientific, New York, USA, supplied all other chemicals and reagents.

2.2. Formulation of rutin-encapsulated chitosan/guar gum nanoparticles (RTN-loaded CS/GG-NPs)

At first, RTN-encapsulated chitosan NPs was formulated using the ionotropic gelation method, followed by coating with guar gum using bifunctional polyethylene glycol [38]. RTN-loaded chitosan nanoparticles (CS-NPs) were prepared by ionic gelation. Briefly, 5 mL of

chitosan solution (pre-dissolving 250 mg of chitosan in 50 mL of 5% glacial acetic acid), with 5 mg of RTN, was subjected to continuous magnetic stirring. An aqueous solution of sodium tripolyphosphate (1.2 mL, 0.5%) was added gradually to the chitosan solution, resulting in the spontaneous formation of RTN-loaded chitosan nanoparticles. The mixture was maintained under magnetic stirring for 52 h. The nanoparticle suspension was then centrifuged at 10,000 rpm for 15 min, and the centrifugation and washing procedure was repeated at least four times. The collected nanoparticles were washed with distilled water and dried. The RTN loading capacity and encapsulation efficiency were subsequently determined using a UV–visible spectrophotometer. To prepare the chitosan/guar gum (CS/GG) nanoparticles system, 20 mg of guar gum was dispersed in 10 mL of distilled water. The pH of the dispersion was adjusted to 5.0 using formic acid, and the mixture was continuously stirred magnetically for 24 h using a Remi magnetic stirrer (Mumbai, India). Subsequently, 250 mg of bifunctional polyethylene glycol (NH_2–PEG–COOH) was incorporated into the guar gum dispersion under continuous stirring. This was followed by the addition of 250 mg of EDAC, and the reaction mixture was allowed to proceed at room temperature for 12 h. After completion of the reaction, the previously formulated RTN-loaded chitosan nanoparticles were dispersed in 10 mL of distilled water and transferred into the guar gum-based polymeric solution. The resulting mixture was continuously stirred for an additional 24 h to facilitate the formation of RTN-loaded CS/GG nanoparticles. The nanoparticle suspension was then sonicated for 15 min using an ultrasound-assisted extractor (PCI Analytics Ltd., Mumbai, India). Subsequently, the suspension was centrifuged at 15,000 rpm for 20 min. The supernatant was carefully discarded, and the resulting pellet was collected, washed, and freeze-dried at −20 °C. The resulting RTN-CS/GG-NPs were further lyophilized for 48 h using a Martin Christ freeze-drying system (Gefriertrocknungsanlagen GmbH). The dried RTN-CS/GG-NPs formulation was collected and stored until further characterization and investigation.

2.3. Encapsulation efficiency (EE) and loading capacity of RTN

The encapsulation efficiency (EE%) and loading capacity (LC%) of RTN in chitosan/guar gum nanoparticles (CS/GG-NPs) were determined using our previously reported method [39], with minor modifications. In brief, 100 mg of newly formulated RTN-encapsulated CS/GG-NPs was dissolved in 10 mL of deionized water and centrifuged at 5000 rpm for 20 min. Following centrifugation, the RTN-encapsulated CS/GG-NPs (unencapsulated) supernatant was carefully recovered. Lastly, the unencapsulated RTN supernatant was analyzed using a UV-visible spectrophotometer (UV-1800, Shimadzu, Japan) at 357 nm. The %EE and %LC of RTN were calculated using the following equations:

$$\%EE \text{ of RTN} = ((RTN)_{added} - (RTN)_{measured})/(RTN)_{added}) \times 100 \quad (1)$$

$$\%LC \text{ of RTN} = ((RTN)_{added} - (RTN)_{measured})/ \text{ weight of the nanoparticle}) \times 100 \quad (2)$$

2.4. *In vitro* drug release of RTN-encapsulated CS/GG-NPs

Based on our earlier investigation, a dialysis-bag diffusion method was used to assess the *in vitro* drug release of RTN from CS/GG-NPs [18]. The drug release study was performed in various pH buffer systems, such as 0.01 M acetate buffer (pH 3.2), 0.01 M phosphate buffer (pH 5.8), and 0.01 M phosphate buffer (pH 7.2). Briefly, 50 mg of RTN-CS/GG-NPs was weighed, transferred to a dialysis membrane bag (MW: 3500 Da, Himedia Laboratories, Mumbai, India), and then properly sealed. After that, the dialysis membrane bag was immersed in a beaker containing 100 mL of various buffer solutions, including acetate buffer at pH 3.2, phosphate buffer at pH 5.8, and phosphate buffer at pH 7.2, and swirled at 150 rpm using a magnetic stirrer held at room temperature. Furthermore, 3 mL of RTN release samples were obtained at various time points. Simultaneously, the same volume of fresh phosphate buffer was added to the beaker, which was then placed under sink conditions. Furthermore, the collected drug release samples were diluted in ethanol and centrifuged at 15,000 rpm for 20 min. Following centrifugation, the concentration of RTN in CS/GG-NPs was determined using

UV-visible spectrophotometry at 357 nm. Finally, the percentage of drug release concentration was estimated using the following formula:

$$\% \text{ drug release of RTN} = ((A_0 - A_1)/ A_0) \times 100 \quad (3)$$

Where A_0 = absorbance of RTN control,

A_1 = absorbance of the RTN tested sample.

2.5. *In vitro* drug release kinetics of RTN-CS/GG-NPs

The *in vitro* drug release data from the aforementioned experiments were utilized for five different unique kinetic models, including zero-order, first-order, Higuchi, Korsmeyer-Peppas, Hixson-Crowell and Hopfenberg models, using the DD Solver program (plug-in for Excel program) to investigate the drug release kinetics and diffusion kinetics mechanism of RTN from CS/GG-NPs. Furthermore, each kinetic model generates a unique drug-release mechanism, including a release rate, a constant, and regression coefficients (r^2) [40].

2.6. Stability studies of RTN-encapsulated CS/GG-NPs

As previously published research, the stability of RTN-CS/GG-NPs was performed under different physiological fluids and buffer solutions, including 10% NaCl, 0.5% bovine serum albumin (BSA), simulated gastric juice and saliva, acetic buffer (pH 3.0 and 5.2), and phosphate buffer (pH 6.4, pH 7.4 and pH 9.0) [41]. Briefly, 0.5 mg of newly formulated RTN-CS/GG-NPs was dissolved in 0.5 mL of each of the above-mentioned physiological medium and buffer solutions, and kept at room temperature. Following various incubation periods, the samples were withdrawn, and the absorbance was measured ranging from 200 to 800 nm using a UV-visible spectrophotometer.

2.7. Physicochemical examination of RTN-CS/GG-NPs

The RTN-encapsulated CS/GG-NPs were characterized in various physicochemical techniques, such as Fourier-transform infrared spectroscopy (FTIR), X-ray diffraction (XRD), Dynamic light scattering (DLS), High-resolution X-ray photoelectron spectroscopy (XPS),

Field Emission Scanning Electron Microscopy (FESEM), and High-resolution transmission electron microscope (HRTEM) analysis. Initially, chemical interactions and functional groups of RTN, CS, GG, and RTN-CS/GG-NPs were identified using FTIR (Shimadzu IR Tracer, Japan). Additionally, FT-IR spectra were recorded in a transmission range of 4000-400 cm^{-1} at a resolution of 4 cm^{-1}. The physical characteristics of RTN, chitosan, and RTN-encapsulated CS/GG-NPs were evaluated using XRD (Bruker D8 Advance, Germany, combined with an SSD160 1-D detector). Moreover, the detector operates in a 2θ configuration at a voltage of 40 kV and an applied current of 30 mA, using Cu Kα1 radiation (λ = 0.1544060). Furthermore, the DLS was used to examine the average particle size (*Z*-average), polydispersity index (PDI), and zeta potential of RTN-CS/GG-NPs using Zetasizer Nano ZS (Malvern Instruments, UK). Initially, the sample was sonicated after the experiment was carried out, and all process performed in Milli-Q water only. In addition, the surface elemental composition and chemical states of RTN-CS/GG-NPs were evaluated using XPS (Thermo Scientific, UK) over the 0-1400 eV range, combined with A1/Ka (hv = 1486.6 eV). Further, the surface structure, shape, and size of RTN-CS/GG-NPs were examined using FESEM (Thermo Fisher Scientific APREO 2SEM, FESEM). Furthermore, 2 mg of RTN-CS/GG-NPs was taken and dissolved in distilled water. Subsequently, 2 µl of the dissolved RTN-CS/GG-NPs sample was placed on a copper mesh grid and observed. Finally, the internal structure and accurate particle size of RTN-CS/GG-NPs were determined using HRTEM (JOEL-2100). In brief, RTN-CS/GG-NPs were dispersed in 1 mL of deionized water, and a few drops of the sample were placed onto a carbon-coated copper grid and observed [42].

2.8. Molecular modeling studies

2.8.1. Potential target prediction of RTN against ovarian cancer

Potential molecular targets of RTN were identified using the SwissTargetPrediction online platform (http://www.swiss-targetprediction.ch/) by submitting the canonical SMILES

structure of RTN and selecting *Homo sapiens* as the target organism. Ovarian cancer-associated genes were retrieved from the GeneCards (http://www.genecards.org/) and DesGenet databases (http://www.disgenet.org/). The target lists obtained from all sources were combined, and identical entries were removed to generate a unified dataset. A Venn diagram was then constructed using the web tool (https://www.interactivenn.net/) to identify the common targets shared between RTN and ovarian cancer. The resulting overlapping genes were further analyzed using bioinformatics tools to investigate the potential molecular mechanisms of RTN against ovarian cancer and to provide a foundation for consequent network pharmacology and functional enrichment analyses [43].

2.8.2. Prediction of Protein–Protein–Interaction Network- and Hub- Genes

The STRING database (https://string-db.org/; accessed on July 15, 2026) was used to analyze protein–protein interactions among the identified hub genes in *Homo sapiens* [44]. The interaction network was visualized using Cytoscape (version 3.10.1), and the CytoHubba plugin was applied to identify hub genes based on network connectivity. Consistent with the findings of Wang et al. (2021), the analysis identified several highly connected genes, suggesting that they may play important roles in underlying biological processes and disease-related signaling networks [45].

2.8.3. Building of Target Compound Pathway Network

Kyoto Encyclopedia of Genes and Genomes (KEGG) pathway enrichment analysis of the identified hub genes was performed using the DAVID (Database for Annotation, Visualization and Integrated Discovery) online platform (https://david.ncifcrf.gov/tools.jsp, accessed on July 15, 2026) [46]. Significantly enriched signaling pathways were identified to elucidate the biological functions and molecular mechanisms connected with the hub genes. Subsequently, a pathway-gene interaction network was built to illustrate connections between

the hub genes and the enriched KEGG pathways, thereby providing insights into potential mechanisms by which the bioactive compound may exert its therapeutic effects.

2.8.4. Gene Ontology and KEGG Pathway Analysis

Gene Ontology (GO) functional annotation and Kyoto Encyclopedia of Genes and Genomes (KEGG) pathway enrichment analyses were performed using the DAVID (Database for Annotation, Visualization and Integrated Discovery) platform, with *Homo sapiens* as the reference organism (http://david.ncifcrf.gov/ accessed on July 15, 2026) [47]. GO analysis was performed to categorize the candidate genes into three functional properties: biological process (BP), cellular component (CC), and molecular function (MF). KEGG pathway analysis was conducted to identify significantly enriched signalling pathways associated with the target genes. Enrichment results with a p-value < 0.05 were considered statistically significant. The top 20 enriched GO terms (BP, CC, and MF) and KEGG pathways were selected for visualization using bar and lollipop plots generated with the ShinyGO web server (http://bioinformatics.sdstate.edu/go/, accessed on July 15, 2026).

2.8.5. Molecular Docking

Molecular docking was performed using the AutoDock Vina docking engine integrated with MGLTools (AutoDockTools) to evaluate the binding interactions between RTN and the key protein targets identified through network pharmacology analysis [48]. The selected target proteins included Estrogen receptor alpha (ESR1) (PDB ID: 1SJ0), Hepatocyte Growth Factor Receptor (c-MET kinase domain) (PDB ID: 3VW8), Myeloid cell leukemia-1 (MCL-1) (PDB ID: 4WMR), Insulin-like growth factor 1 receptor (IGFR-1R) (PDB ID: 5FXQ), Tumor Necrosis Factor-alpha (TNF-α) (PDB ID: 7JRA), Tumor Necrosis Factor-alpha (hTNF-α) (PDB ID: 7KP9), Transformation-related protein 53 (TP53) (PDB ID: 8F0W), Epidermal Growth Factor Receptor kinase domain (EGFR) (PDB ID: 8F1X), Matrix Metalloproteinase-9 (MMP-9) (PDB ID: 8K5W), Heat shock protein 90 beta (HSP90AB1) (PDB ID: 8W8K), and

Matrix Metalloproteinase-2 (MMP-2) (PDB ID: 8H78). Protein structures were obtained from the Protein Data Bank and prepared by removing water molecules and co-crystallized ligands, followed by the addition of polar hydrogen atoms and Kollman charges. The three-dimensional structure of RTN was prepared and converted into the required docking format using AutoDock Tools. The docking grid was centred on the experimentally reported ligand-binding pocket of each protein. Grid boxes were generated with approximately 5 Å of additional space surrounding the active site to ensure complete coverage of the binding region. Docking studies were performed with an exhaustiveness value of 8. The remaining parameters were kept at their default settings, including a grid spacing of 1.0 Å, 9 output binding modes, and an energy range of 3 kcal/mol. The predicted binding affinities (kcal/mol) were used to assess the binding strength of RTN toward each target protein. The highest-ranked docking conformations were further examined to identify hydrogen-bonding and hydrophobic interactions within the active-site residues, providing insights into the molecular basis of ligand-protein binding.

2.8.6. Molecular Dynamics Simulation

Molecular dynamics (MD) simulations were performed using the Desmond v6.3 module of the Schrödinger software suite with the OPLS-2005 force field to evaluate the stability of the five top-scoring protein-ligand complexes obtained from molecular docking studies. Each complex was placed in an orthorhombic simulation box and solvated using the Transferable Intermolecular Potential with 3 Points (TIP3P) water model. The system was neutralized by adding appropriate counterions, and 0.15 M NaCl was introduced to mimic physiological ionic strength. Before the simulation run, the systems underwent energy minimization, followed by a standard relaxation protocol consisting of equilibration steps at predefined temperature and pressure. Initially, the top-scored five protein-ligand complexes underwent a 10 ns MD simulation to provide a preliminary assessment. Based on the stability of the complexes, 100 ns simulations were performed for detailed analysis. All simulations were carried out in the

Number of particles (N), Pressure (P), and Temperature (T) (NPT) ensemble at 300 K and 1.01325 bar, with periodic boundary conditions. The stability and dynamic behavior of each protein-ligand complex were evaluated by analyzing the root-mean-square deviation (RMSD), root-mean-square fluctuation (RMSF), and protein-ligand interaction profiles throughout the simulation period. In addition, hydrogen bonds, hydrophobic interactions, ionic interactions, and water-mediated contacts between the ligand and amino acid residues were assessed to examine the stability and binding characteristics of the protein–ligand complexes. These analyses provided a thorough understanding of the ligand's structural stability and dynamic interactions within the protein binding pocket during the simulation [49].

2.9. Anticancer studies of RTN-CS/GG-NPs

2.9.1. Cytotoxicity

The human SKOV-3 ovarian cancer cell line and the fibroblast cell line (L929) were used to evaluate the cytotoxic activity and biocompatibility of RTN-CS/GG-NPs, respectively [50]. In brief, SKOV-3 ovarian cells and L929 cells were grown in a T25 flask with Dulbecco's Modified Eagle Medium (DMEM) supplemented with 10% Fetal Bovine Serum (FBS) and antibiotics (1% amphotericin B, 1% penicillin, and 1% streptomycin), and maintained at 37°C for 24 h in 5% CO_2. Following incubation, an inverted microscope (Olympus, Japan) was used to regularly monitor cell morphology and contamination. After the cells reached 70–80% confluency, the previous medium was discarded, and the cells were rinsed twice with 1× PBS. After that, 0.25% trypsin-EDTA was added to the flask (to detach the cells), and the flask was maintained at 37°C in 5% CO_2 for 2-3 min. After incubation, the cells were observed with an inverted microscope. Then, the cells were detached immediately after trypsin neutralization using medium supplemented with 10% FBS. Furthermore, the suspensions were collected in a tube and centrifuged at 1000 rpm for 5 min. After centrifugation, the pellet was obtained and reconstituted in a fresh medium. Further, the exact number of cells was counted using a Trypan

blue exclusion test (Automated cell counter, Thermo Fisher Scientific, USA). After counting, the suspension was precisely diluted, and cells were grown in a plate at 37°C with 5% CO_2 for 24 h. Later, using the 3-[4,5-dimethylthiazole-2-yl]-2,5-diphenyltetrazolium bromide (MTT) assay, the cytotoxic effects and cellular viability of RTN-CS/GG-NPs were evaluated against SKOV-3 ovarian cancer cells and L929 cells. In summary, SKOV-3 and L929 cells were grown in a 96-well plate in triplicate (Tarson India Pvt. Ltd., India) at a density of 5×10^3 cells/well and incubated at 37°C in 5% CO_2 for 24 h. Following incubation, the medium was discarded, the flask was rinsed twice with 1× PBS, and the flask was replaced with fresh DMEM. The cells were then exposed to various concentrations of RTN-CS/GG-NPs (0.1, 0.5, 1, 5, 10, 25, 50, 75, and 100 µg/mL) and free RTN (0.1, 0.5, 1, 5, 10, 25, 50, 75, and 100 µg/mL) at 37°C in 5% CO_2 for 24 h and 48 h. Following treatment, cells were washed in the old medium, rinsed twice in 1 x PBS, and the DMEM medium was replaced. To create formazan crystals, 20 µL of MTT (5 mg/mL) stain was added directly to each well and incubated at 37°C with 5% CO_2 for 4 h in the dark. Following incubation, the excess MTT-stained medium was discarded, and the plate was washed twice with PBS. Further, DMSO was added to each well (to dissolve the formazan crystals). Furthermore, absorbance was measured at 570 nm and 630 nm using a microplate spectrophotometer (MultiskanGO, Thermo Scientific, USA). Also, the percentage of cell viability was evaluated using the following formula:

$$\% \text{ cell viability} = (\text{Absorbance}_{\text{test-blank}}/\text{Absorbance}_{\text{control-blank}}) \times 100 \quad (4)$$

2.9.2. Examination of the apoptosis assay using Acridine Orange/Ethidium Bromide (AO/EB) staining

The programmed cell death of RTN-CS/GG-NPs in SKOV-3 ovarian cancer cells was assessed using AO/EB dual staining [51]. In brief, cells were grown in a 6-well plate at a density of 5×10^4 cells/well and kept at 37°C with 5% CO_2 for 24 h. Following incubation, the cells' old medium was discarded, and the cells were washed twice with 1× PBS. The SKOV-3

cells were subsequently exposed to an IC_{50} concentration of RTN-CS/GG-NPs and maintained at 37°C with 5% CO_2 for 24 h. Following treatment, the medium was discarded, and the wells were rinsed. 50 µL of dual fluorescent stain (100 µg/mL AO/100 µg/mL EB) was added to each well, and the wells were kept at 37°C in 5% CO2 in the dark. After incubation, the excess stained medium was discarded, the slide was washed, and the stained suspension was placed on a microscope slide and visualized at 20X magnification using a Trinocular inverted phase-contrast fluorescence microscope (Carl Zeiss Axiovert 40 CFL, Germany). Thus, a green nucleus indicates living cells; a bright green nucleus or bright green spots indicate early apoptotic cells; an orange/yellow nucleus indicates late apoptotic cells; and an orange to red nucleus indicates necrotic or induced cell death.

2.9.3. Evaluation of nuclear condensation using 4′,6-diamidino-2-phenylindole (DAPI) staining

4′,6-diamidino-2-phenylindole **(**DAPI) staining was used to assess changes in nuclear morphology or condensation in RTN-CS/GG-NPs compared with SKOV-3 ovarian cancer cells [52]. Briefly, the SKOV-3 cells were seeded on sterile glass coverslips, transferred to a 6-well plate at a density of 5×10^4 cells/well, and maintained at 37°C with 5% CO_2 for 24 h. After that, the cells' old medium was removed, and the cells were washed twice with 1× PBS. Moreover, the cells were treated with RTN-CS/GG-NPs at an IC50 concentration for 24 h. Following treatment, the medium was discarded and washed twice. Further, the cells were fixed with 4% paraformaldehyde for 15 min and kept at room temperature. Then, the fixed cells were washed and permeabilized using 0.1% Triton X for 10 min. Following permeabilization, the cells were stained with DAPI solution (1 µg/mL) at 37°C for 10 min in the dark. Following the incubation period, the excess stained medium was discarded, and the remaining medium was rinsed with 1× PBS. Further, the coverslips were mounted on a glass slide. Finally, the cells'

nuclear changes were visualized at 20X magnification with a fluorescence microscope using a DAPI filter, with excitation at 358 nm (λex) and emission at 461 nm (λ_{em}).

2.9.4. Examination of the reactive oxygen species (ROS) levels using 2′,7′-dichlorodihydrofluorescein diacetate (DCFH-DA)

2′,7′-dichlorodihydrofluorescein diacetate (DCFH-DA) was used to assess intracellular reactive oxygen species (ROS) levels in RTN-CS/GG-NPs against SKOV-3 ovarian cancer cells [53]. In brief, SKOV-3 cells were seeded in a 6-well plate at a density of 5×10^4 cells/well and treated with RTN-CS/GG-NPs at an IC50 concentration for 24 h. Following treatment, the medium was discarded, and the cells were stained with 10 µM DCFH-DA at 37°C for 30 min in the dark. Following the incubation period, the excess stained medium was discarded and rinsed. Finally, intracellular ROS levels were visualized at 20X magnification using a fluorescence microscope with a FITC (Fluorescein Isothiocyanate) filter, with excitation at 488 nm (λex) and emission at 525 nm (λ_{em}). Further, ImageJ software (National Institute of Health, USA) was used to measure the mean fluorescence intensity (MFI).

2.9.5. Evaluation of Mitochondrial Transmembrane Potential (ΔΨm)

Rhodamine 123 was used to examine the loss of mitochondrial transmembrane potential (ΔΨm), metabolic and cellular activities of RTN-CS/GG-NPs in SKOV-3 ovarian cancer cells [54]. Initially, the cells were seeded in a 6-well plate at a density of 5×10^4 cells/well, and kept at 37°C in 5% CO_2 for 24 h. Then, the cells were treated with an IC_{50} concentration of RTN-CS/GG-NPs and maintained for 24 h. After that, the medium was discarded, washed, and replaced with DMEM. Additionally, all cells were stained with 10 µg/mL Rhodamine 123 and incubated at 37°C for 30 min. After discarding and washing the staining solution, the cells were examined under a fluorescence microscope with an FITC filter at 20X magnification, with excitation at 488 nm (λ_{ex}) and emission at 525 nm (λ_{em}).

2.9.6. Wound scratch assay in SKOV-3 cells

The migratory ability of RTN-CS/GG-NPs was examined in SKOV-3 ovarian cancer cells using a wound-healing scratch assay [55]. Briefly, the cells were grown in a 6-well plate at a density of 5×10^4 cells/well and maintained at 37°C in 5% CO_2 for 24 h. Subsequently, a consistent wound was created on a cell monolayer utilizing a sterile pipette tip. Furthermore, the cells were exposed to an IC_{50} concentration of RTN-CS/GG-NPs for varying durations. Initially, the wound area was immediately captured using an inverted phase-contrast microscope for 0^{th} h. Following incubation, additional images were collected of the same wound area at various time intervals, such as after 24^{th} h and 48 h, until the end of the wound closure in the cells. Additionally, the wound width was measured at different time points, and cell migration into the wound region was quantified using ImageJ software (National Institutes of Health, USA). Furthermore, the percentage of wound closure was measured by the given formula:

% wound closure = Initial wound width – Final wound width/ Initial wound width × 100 (5)

2.10. Statistical Analysis

All statistical data analysis was conducted using SPSS statistical software 20.0 (SPSS Inc., IL, USA). Furthermore, drug release, cell viability, and scratch assay were among the experimental studies that employed mean ± standard deviation (SD). One-way ANOVA (Analysis of Variance) and two-way ANOVA, with Tukey's multiple comparison test. All experiments were performed at least three times, with a statistically significant p-value < 0.05.

3. Results

3.1.Formulation of RTN-CS/GG-NPs

RTN-CS/GG-NPs was prepared through the ionic gelation technique. The successful incorporation of RTN into the CS NPs matrix was confirmed by UV–visible spectroscopy, which showed the disappearance of the characteristic absorption peak of free RTN (Figure 1). Later, RTN-loaded CS NPS were coated with guar gum to form RTN-CS/GG-NPs. The

nanoparticles exhibited a loading capacity of 9.88 ± 0.74% and an encapsulation efficiency of 86.71 ± 1.35%. The high encapsulation efficiency, together with the relatively low loading capacity, suggests that RTN has a strong affinity for the chitosan matrix.

3.2.Drug release and release kinetics studies

The *in vitro* release behavior of RTN from CS/GG-NPs was evaluated using a dialysis membrane bag in 0.01 M acetate buffer (pH 3.2) and 0.01 M phosphate buffer solutions (pH 5.8 and 7.2) at 37°C. The cumulative drug release profiles are presented in Figure 2. During the initial 8 h, RTN release reached 22.12 ± 1.72% at pH 3.2, 30.57 ± 1.19% at pH 5.8, and 28.55 ± 0.99% at pH 7.2, indicating a relatively faster release under mildly acidic conditions. Over the course of the study, the highest cumulative release was observed at pH 5.8, reaching 83.27 ± 0.56% within 40 h. In comparison, the cumulative release at pH 3.2 was 71.43 ± 0.33% after 40 h, while at pH 7.2 it reached 81.13 ± 0.32% within 44 h. These findings suggest that the release of RTN from CS/GG-NPs is influenced by the pH of the surrounding medium, with the greatest drug release occurring at pH 5.8. The release kinetics of RTN from CS/GG-NPs were evaluated using various mathematical models, including zero-order, first-order, Higuchi, Korsmeyer–Peppas, Hixson–Crowell, and Hopfenberg (Table 1). For each model, the release rate constant, Akaike Information Criterion (AIC) and coefficient of determination (r^2) were calculated to identify the model that best described the drug-release behavior. An r^2 value near 1 indicates a better agreement between the experimental data and the fitted model. Among the evaluated models, the first-order kinetic model showed better correlation than the zero-order model at all tested pH conditions. The first-order model r^2 values at pH 7.2 (0.9804 to 0.8641), pH 5.8 (0.9824 to 0.8636), and pH 3.2 (0.9828 to 0.8933) were greater than those for zero-order kinetics, according to the kinetic model analysis. The Higuchi model also demonstrated a strong correlation with the experimental data, with r^2 values of 0.9822 at pH 7.2, 0.9644 at pH 5.8, and 0.9626 at pH 3.2. The high linearity of the Higuchi plots indicates that diffusion

was the primary mechanism controlling RTN release from the CS/GG nanoparticles. The Korsmeyer–Peppas model further supported the release mechanism. The release exponent (n) values were 0.611 at pH 3.2, 0.570 at pH 5.8, and 0.498 at pH 7.2. These values suggest that drug release occurred mainly through anomalous (non-Fickian) transport, involving a combination of diffusion and polymer relaxation or swelling. The value at pH 7.2 ($n \approx 0.498$) is close to the Fickian diffusion limit, indicating that diffusion was the dominant release mechanism under these conditions. Overall, the kinetic analysis indicates that RTN release from CS/GG nanoparticles was best described by the first-order and Higuchi models. These findings suggest that drug release was concentration-dependent and primarily governed by diffusion through the polymeric matrix, resulting in a controlled and sustained release profile.

3.3.Stability studies

Figure 3 illustrates the in vitro stability of the developed RTN-CS/GG nanoparticles (NPs) after 120 h of incubation in physiological medium and different buffer solutions. The NPs showed a characteristic maximum absorbance between 410 and 420 nm under all tested conditions. A slight bathochromic shift of approximately 10 nm in the absorption maximum was observed at neutral pH in the physiological medium and buffer system, suggesting that the RTN-CS/GG-NPs maintained good physicochemical stability under these conditions.

3.4.Physicochemical Characterization of RTN-CS/GG-NPs

FTIR spectral analysis is an important analytical technique for understanding the interaction between the loaded drug and the nanocarrier system. The FTIR spectra of guar gum, RTN, chitosan, and RTN-CS/GG-NPs (Figure 4), along with their major peaks and corresponding functional groups, are presented in Table 2. The observed RTN-CS/GG-NPs spectra showed functional groups: -OH (3666), -NH (3416), C-H (2766), O=C=O (2333), C=N (2083), and C=C (1666). These observed functional groups in the formulated NPs were derived from RTN, chitosan, and guar gum. These results indicate that RTN is encapsulated and

stabilized by chitosan and guar gum. The X-ray diffraction spectroscopy (XRD) analysis revealed the physical nature of free RTN (Figure 5(a)), Chitosan (Figure 5(b)), and RTN-CS/GG-NPs (Figure 5(c)), specifically their crystallinity, amorphousness, atomic spacing, and phase composition. The diffraction pattern of pure RTN exhibited several intense, well-defined peaks at distinct 2θ values, confirming its crystalline structure. Chitosan displayed characteristic diffraction peaks at approximately 12° and 29° (2θ), along with a broad diffraction band, indicating its semi-crystalline nature. The XRD pattern of the RTN-CS/GG-NPs showed characteristic diffraction peaks at approximately 32° and 46° (2θ), suggesting that the nanoparticle formulation retained a semi-crystalline structure. Compared with the diffraction pattern of free RTN, slight shifts in the peak positions were observed after drug encapsulation within the CS/GG polymeric matrix. The observed changes in the diffraction pattern confirm the successful incorporation of RTN within the CS/GG polymeric matrix and indicate the formation of interactions between the drug and the polymer chains. Despite these changes, the nanoparticles retained their semi-crystalline structure. Furthermore, the absence of the characteristic diffraction peaks of free RTN in the RTN-CS/GG NP diffractogram suggests that the drug was effectively entrapped within the semi-crystalline polymer network, thereby reducing crystallinity and stabilizing the nanoparticle system. The intensity-weighted mean particle size (Z-average) and zeta potential of the freshly prepared RTN-CS/GG nanoparticles (NPs) are shown in Figure 5(d) and Figure 5(e), respectively. The average hydrodynamic diameter of the nanoparticles, measured immediately after formulation in deionized water, was 42.76 nm, indicating a narrow particle-size distribution in the suspension. The zeta potential of the freshly prepared RTN-CS/GG-NPs was found to be +57.6 mV, reflecting a highly positive surface charge. This high zeta potential value suggests strong electrostatic repulsion between the nanoparticles, contributing to good colloidal stability and minimizing particle aggregation during storage. Figure 5(f) shows the high-resolution X-ray

photoelectron spectroscopy (XPS) survey spectrum of the prepared RTN-CS/GG nanoparticles (NPs). The surface elemental composition of the nanoparticles was verified using the characteristic signals from carbon (C 1s), nitrogen (N 1s), and oxygen (O 1s). The prominent C1s peak observed at approximately 285 eV is attributed to C–C and C=C bonds present in the polysaccharide backbone of chitosan and guar gum. The N1s peak, centred around 402 eV, corresponds to C–N functional groups associated with the amino groups of the polymeric matrix. In addition, the O1s peak detected near 543 eV is assigned to oxygen-containing functional groups, including C–O–H and O=C bonds, which originate from the hydroxyl and carbonyl functionalities of the CS/GG polymer network. These characteristic binding energies confirm the successful formation of the RTN-CS/GG-NPs system and the presence of the expected surface chemical functionalities. The morphology and particle size of the RTN-CS/GG nanoparticles (NPs) were characterized using field-emission scanning electron microscopy (FESEM) and high-resolution transmission electron microscopy (HRTEM). As shown in Figures 6(a)–6(c), FESEM micrographs at different magnifications revealed that the formulated nanoparticles were predominantly spherical and exhibited a relatively uniform surface morphology. The particle size estimated from the FESEM images ranged from approximately 100 to 200 nm. The HRTEM micrographs (Figures 6(d)–6(f)) further confirmed the spherical morphology of the nanoparticles and revealed particle diameters ranging from 80 to 200 nm. The close agreement between the FESEM and HRTEM observations supports the successful formation of well-defined RTN-CS/GG nanoparticles with nanoscale dimensions.

3.5.Molecular modeling studies

3.5.1. Targets Related to RTN and Ovarian Cancer

A total of 100 potential RTN targets were obtained from the SwissTargetPrediction database (Supporting Information). In addition, 16,812 genes associated with ovarian cancer were collected from the GeneCards database (Supplementary File 1). To identify shared

606 targets, an interactive Venn diagram analysis was performed by comparing RTN-related targets
607 with ovarian cancer-associated genes. The analysis identified 93 overlapping genes as potential
608 therapeutic targets. These common genes were selected as hub genes that may contribute to
609 RTN's therapeutic effects against ovarian cancer, as illustrated in Figure 7(a).

610 **3.5.2. Protein-Protein Interaction Analysis**

611 The protein-protein interaction (PPI) network of the 93 shared targets was constructed
612 using the STRING database (version 11.0), with the analysis restricted to *Homo sapiens*. A
613 high-confidence interaction score of ≥0.7 was applied to ensure reliable interactions. Multiple
614 evidence sources, including experimental studies, curated databases, co-expression, gene
615 neighbourhood, gene fusion, and co-occurrence, were incorporated into the analysis. Nodes
616 that showed no interactions within the network were excluded from further investigation. The
617 resulting PPI network was imported into Cytoscape (version 3.10.4) for visualization and
618 network analysis. Topological properties of the network were evaluated using the Network
619 Analyzer tool, including degree, betweenness centrality, clustering coefficient, network
620 density, characteristic path length, and network heterogeneity. In addition, spectral graph
621 theory was applied to automatically partition the weighted interaction matrix, and the
622 corresponding results are presented in Supplementary File 1. The constructed network
623 consisted of 95 nodes and 461 edges, revealing several densely connected clusters that may
624 represent biologically important functional modules (Figure 7(b)). To identify the most
625 influential genes within the network, the CytoHubba plugin in Cytoscape was employed. Hub
626 genes were ranked using multiple topological algorithms, including Degree, Betweenness,
627 Closeness, Edge Percolated Component (EPC), Radiality, Stress, Bottleneck, Eccentricity,
628 Clustering Coefficient, Density of Maximum Neighborhood Component (DMNC), Maximum
629 Neighborhood Component (MNC), and Maximum Clique Centrality (MCC). Among these
630 methods, MCC was selected as the primary ranking criterion because of its effectiveness in

identifying essential proteins in complex biological interaction networks. Based on the highest MCC scores, 10 hub genes were identified: ESR1, MCL1, MET, TP53, IGF1R, TNF, EGFR, HSP90AB1, MMP9, and MMP2. These genes occupied central positions within the interaction network and exhibited strong connectivity, suggesting their potential importance in the therapeutic mechanism of RTN against ovarian cancer (Figure 7(c)).

3.5.3. Molecular docking

Docking experiments have shown that RTN is an effective molecule for 11 proteins associated with ovarian cancer by precisely mimicking essential recognition motifs present in their cocrystal ligands and, in several instances, achieving higher binding scores (Table 3). Figure 8 depicts the 3D and 2D images of RTN interacting with all 11 proteins. In ESR1 (PDB ID: 1SJ0), RTN had a binding score of -9.2 kcal/mol, higher than the cocrystal value of -9.1 kcal/mol. It also maintained important hinge connections with PHE404, GLU353, and CYS530. RTN replaced CYS530 in the co-crystal ligand with the stable HIE 524. RTN had a binding score of -6.4 kcal/mol for Hepatocyte Growth Factor Receptor (c-MET kinase domain)(MET) (PDB id: 3VW8), which is lower than the value of -8.2 kcal/mol for cocrystal (N-({4-[(6,7-dimethoxyquinolin-4-yl)oxy]phenyl}carbamothioyl)-2-phenylacetamide). It is maintained important hinge connections with PHE1223 and ASP1231.

For MCL-1 (PDB id: 4WMR), RTN's binding score was -7.8 kcal/mol and the cocrystal (7-[2-(1H-imidazol-1-yl)-4-methylpyridin-3-yl]-3-[3-(naphthalen-1-yloxy)propyl]-1-[2-oxo-2-(piperazin-1-yl)ethyl]-1H-indole-2-carboxylic acid) score very close -7.7 kcal/mol. It is maintained important hinge connections with ARG263 and LEU246. RTN against IGFR-1R (PDB id: 5FXQ) showed a score of -8 kcal/mol, involving contacts with the important amino acids MET1082 and ASP1086 of the protein. In contrast, the co-crystal (5-chloranyl-4-imidazo[1,2-a]pyridin-3-yl-N-(5-methyl-1-piperidin-4-yl-pyrazol-4-yl)pyrimidin-2-amine) score was - 6.5 kcal/mol with MET1082. TNF-ALPHA (PDB id: 7JRA), RTN's binding score

656 was -5.7 kcal/mol, and the cocrystal (2-[5-(3-chloro-4-{[(1R)-1-(2-
657 fluorophenyl)ethyl]amino}quinolin-6-yl)pyrimidin-2-yl]propan-2-ol) score was -8.6 kcal/mol
658 compared to RTN, which involves contact with important amino acids TYR135 and ILE123
659 of the protein. The same, TNF-ALPHA (PDB id: 7KP9), RTN's binding score was -6.1
660 kcal/mol and the cocrystal (1-{[2-(difluoromethoxy)phenyl]methyl}-2-methyl-6-[6-
661 (piperazin-1-yl)pyridin-3-yl]-1H-benzimidazole) score lower -5.4 kcal/mol than RTN, which
662 involves contact with important amino acids TYR59, ILE58, and LEU57of the protein. For
663 TP53 (PDB id: 8F0W), RTN's binding score was -6.3 kcal/mol, and the cocrystal (1-[4-(4-
664 ethylpiperazin-1-yl)-3-fluorophenyl]butan-1-one) score was higher -7.9 kcal/mol than that of
665 RTN, which involves contact with important amino acids TYR1502, MET1584, and TRP1495
666 of the protein. For Epidermal Growth Factor Receptor kinase domain (EGFR) (PDB id: 8F1X),
667 RTN's binding score was -7.8 kcal/mol and the cocrystal (propan-2-yl 2-[[4-[2-
668 (dimethylamino)ethyl-methyl-amino]-2-methoxy-5-(propanoylamino)phenyl]amino]-4-(1-
669 methylindol-3-yl)pyrimidine-5-carboxylate) score higher -9.2 kcal/mol than RTN, which
670 involves contact with important amino acids ASN842, ASP800, LEU718, GLU762, and
671 MET793 of the protein. RTN lowers the cocrystal binding in Matrix Metalloproteinase-9 (PDB
672 id: 8K5W), scoring − 7.9 kcal/mol, lower than the co-crystal ligand (2-[[5-fluoranyl-7-
673 (methylamino)-1H-indol-2-yl]carbonyl]-N-(2-pyrrol-1-ylethyl)-3,4-dihydro-1H-isoquinoline-
674 7-carboxamide) score of -8.2 kcal/mol. It contacted GLY233, PHE110, and ASP103 with the
675 target protein. RTN increased cocrystal binding in HSP90AB1 (PDB ID: 8W8K), scoring -8.2
676 kcal/mol, higher than the co-crystal ligand (5-[2,4-dihydroxy-5-(propan-2-yl)phenyl]-4-(1-
677 methyl-1H-indol-5-yl)-2,4-dihydro-3H-1,2,4-triazol-3-one) score of -7.1 kcal/mol. It contacted
678 GLY132, GLY135, GLY37, GLY108, and LYS58 with the target protein. Similarly, RTN
679 increased the cocrystal binding in Matrix Metalloproteinase-2 (PDB id: 8H78), scoring - 9.3
680 kcal/mol, lower than co-crystal ligand ((2~{R})-2-[[4-[(4-

aminocarbonylphenyl)carbonylamino]phenyl]sulfonylamino]-5-[(2~{S},4~{S})-4-azanyl-2-[[(2~{S})-1-[[(2~{S})-1-[(5-azanyl-5-oxidanylidene-pentyl)amino]-5-oxidanyl-1,5-bis(oxidanylidene)pentan-2-yl]-methyl-amino]-4-methyl-1-oxidanylidene-pentan-2-yl] carbamoyl] pyrrolidin-1-yl]-5-oxidanylidene-pentanoic acid) score of -6.8 kcal/mol. It contacted TYR143 and HIS121with the target protein. To confirm pose stability (ligand/protein RMSD, critical H-bond/π-stacking occupancy), we performed brief molecular dynamics simulations on all five complexes (ESR1, IGFR-1R, TNF-ALPHA, MMP9, and HSP90AB1) based on these cocrystal-like interaction patterns and competitive scores.

3.5.4. Molecular dynamics simulation

Molecular dynamics (MD) simulations were performed to further assess the stability of the protein-ligand complexes identified by molecular docking. Initially, all five RTN-protein complexes were subjected to 10 ns MD simulations. Complexes exhibiting stable RMSD and RMSF profiles together with preserved protein-ligand interactions were selected for extended 100 ns simulations. Among these, the RTN-ESR1 complex (PDB ID: 1SJ0) exhibited favourable stability and was selected for detailed analysis. During the 100 ns simulation, the ESR1 backbone RMSD increased early in the trajectory, reaching approximately 3.5 Å, and subsequently stabilized around 3.8 Å for the remainder of the simulation (Figure 9(a)). In comparison, the ligand RMSD remained relatively low throughout the simulation, fluctuating between 0.8 and 2.0 Å, indicating that RTN maintained a stable binding orientation within the active site. RMSF analysis showed only minor fluctuations in amino acid residues, suggesting that ligand binding did not induce substantial structural changes in the protein. Protein-ligand interaction analysis further demonstrated that key binding residues were maintained throughout the simulation period (Figure 9(b)). The residues GLU353, MET421, PHE404, and THR347 exhibited interaction occupancies of 100%, 75%, 68%, and 32%, respectively, highlighting their important roles in stabilizing the RTN-ESR1 complex (Figure 9(e)). In addition, the

interaction timeline (Figure 9(c)) illustrated the persistence of hydrogen bonds, hydrophobic contacts, ionic interactions, and water-mediated bridges during the simulation (Figure 9(d)). Overall, the MD simulation results support the stability of the RTN-ESR1 complex and reinforce the molecular docking findings. These observations suggest that RTN is a promising candidate for further experimental investigation as a potential ESR1 inhibitor and may serve as a useful anti-ovarian cancer target for future drug development studies.

3.6.Anticancer studies

3.6.1. Cytotoxicity studies

Guided by the findings of the molecular docking and molecular dynamics simulation studies, the *in vitro* cytotoxic activity of RTN-CS/GG nanoparticles (NPs) and free RTN was evaluated against SKOV-3 human ovarian cancer cells and L929 mouse fibroblast cells. Both the free-RTN and RTN-CS/GG-NPs were tested at concentrations ranging from 0.1 to 100 µg/mL for incubation periods of 24 and 48 h. After 24 and 48 h of treatment with RTN and RTN-CS/GG-NPs, concentration- and time-dependent reductions in SKOV-3 cell viability were observed (Figures 10(d) and 10(h)), respectively. At the highest tested concentration (100 µg/mL), the percentage of viable cells decreased to 25.67 ± 2.41% after 24 h and further declined to 18.18 ± 1.09% following 48 h of exposure. In comparison, treatment with an equivalent concentration of free-RTN resulted in 39.55 ± 1.19% cell viability after 24 h and 37.14 ± 1.91% after 48 h. These findings demonstrate that RTN-CS/GG-NPs exhibited greater cytotoxic efficacy against SKOV-3 cells than the free-RTN, indicating that nanoparticle encapsulation enhanced RTN's antiproliferative activity. These findings suggest that encapsulating RTN within the CS/GG-NPs system enhances its anticancer activity against SKOV-3 cells while preserving low toxicity toward noncancerous fibroblast cells. The IC_{50} value for RTN-CS/GG-NPs was 23.6 µg/mL and 10.43 µg/mL for 24 h and 48h, respectively. The results of the MTT assay of SKOV-3 cells (Figures 10(a)-(g)) and L929 cells (Figures 10

(i)-(k)) indicate morphological changes after treatment with IC_{50} concentrations of free-RTN and RTN-CS/GG-NPs. In contrast, both free-RTN and RTN-CS/GG-NPs exhibited minimal cytotoxicity toward normal L929 mouse fibroblasts. Following 24 h of treatment at a concentration of 100 μg/mL, free RTN maintained 95.64 ± 0.52% cell viability, whereas RTN-CS/GG-NPs showed 93.87 ± 0.64% cell viability (Figure 10(l)).

3.6.2. Acridine orange (AO) and ethidium bromide (EB) double staining apoptosis study

The AO/EB staining assay was used to assess the apoptotic effects of RTN-CS/GG-NPs and free RTN at IC50 values in SKOV-3 after a 24 h exposure. After 24 h of treatment with NPs and free-RTN at the IC_{50} concentrations, the cells were separated and stained with AO/EB. The dual staining was evaluated under a fluorescence microscope. Figure 11(a) shows no significant apoptosis in the negative control cells. In contrast, cells treated with RTN-CS/GG-NPs and free-RTN exhibited a range of shapes, from spherical to irregular, characterized by condensed nuclei, distorted cell membranes, and apoptotic bodies (Figures 11(b) and 11(c), respectively).

3.6.3. 4′,6-diamidino-2-phenylindole (DAPI) staining

As shown in Figures 11(e) and 11(f), marked alterations in nuclear morphology and chromatin organization were observed in SKOV-3 cells following treatment with free RTN and RTN-CS/GG-NPs compared with the untreated control (Figure 11(d)). Control cells displayed intact, round nuclei with uniform blue fluorescence, indicating normal nuclear architecture. In contrast, treated cells exhibited bright fluorescence, condensed chromatin, nuclear deformation, and irregular cellular morphology, all characteristic features of apoptotic cell death.

3.6.4. Reactive Oxygen Species (ROS) generation of RTN-CS/GG-NPs

Figure 11(g) shows that the untreated SKOV-3 cells exhibited reduced ROS production, and Figures 11(h) and 11(i) show the increased ROS levels by free RTN, and RTN-CS/GG-

NPs. The present study demonstrated that the ability of free RTN and RTN-CS/GG-NPs to generate higher levels of ROS could be exploited in cancer cells (Figures 11(h) and 11(i)) using the DCFH-DA staining technique.

3.6.5. Mitochondrial transmembrane potential damage of RTN-CS/GG-NPs

As illustrated in Figures 11(k) and 11(l), exposure of SKOV-3 cells to free RTN and RTN-CS/GG-NPs at their respective IC_{50} concentrations caused a marked reduction in mitochondrial membrane potential compared with the untreated control (Figure 11(j)). The reduction was more pronounced in cells treated with RTN-CS/GG-NPs, indicating greater mitochondrial membrane depolarization. These findings suggest that the nanoparticle formulation exerts a stronger effect on mitochondrial function than the free drug.

3.6.6. Wound Scratch assay

As shown in Figures 12(d) to 12(f) and Figures 12(g) & 12(i), RTN-CS/GG-NPs and free RTN reduced the migratory ability of SKOV-3 cells compared with the untreated control (Figures 12(a) to 12(c), respectively. In the control group, the wound area gradually decreased from 290480.3 ± 270.5 μm^2 at 0 h to 54874.67 ± 849.85 μm^2 at 24 h and 655 ± 11.53 μm^2 at 48 h, indicating rapid closure of the wound scratch (Figure 12 (i)). In cells treated with free RTN at ½ IC_{50} concentration, the wound area remained comparatively larger, measuring 260691.3 ± 660.65 μm^2, 283330 ± 3216.78 μm^2, and 284232 ± 2073.23 μm^2 at 0, 24, and 48 h, respectively (Figure 12(l)). Similarly, treatment with RTN-CS/GG-NPs at ½IC_{50} resulted in wound areas of 298096 ± 455.66 μm^2, 277646.3 ± 2.081666 μm^2, and 243831.7 ± 584.382 μm^2 at the corresponding time points (Figure 12(k)). The persistence of a larger wound area in the treated groups indicates that both free RTN and RTN-CS/GG-NPs effectively inhibited SKOV-3 cell migration, with the RTN-CS/GG-NPs formulation exhibiting a stronger anti-migratory effect than the untreated control.

4. Discussion

781 This study investigated the anticancer potential of RTN-encapsulated CS/GG-NPs against
782 ovarian cancer cells (SKOV-3 cells). RTN is a naturally occurring polyphenolic flavanol
783 glycoside compound widely found in fruits, vegetables, cereals, and other plant-based sources
784 [56]. RTN, commonly referred to as vitamin P, exhibits a wide range of biological activities,
785 including antioxidant, anti-inflammatory, antiangiogenic, antiproliferative, and pro-apoptotic
786 effects, which are considered beneficial in cancer prevention and treatment [27]. Evidence from
787 earlier reported studies indicates that RTN can inhibit the growth of ovarian cancer cells by
788 interfering with molecular signaling pathways involved in tumour progression [57]. It has also
789 been reported to trigger apoptosis and block harmful cell-signaling processes associated with
790 cancer development. These findings suggest that RTN may be a promising natural compound
791 for developing novel therapeutic approaches against ovarian cancer [58]. Although RTN
792 exhibits a wide range of biological activities, its clinical application via oral administration is
793 limited by its poor aqueous solubility and low bioavailability at the target site [28]. While *in*
794 *vitro* studies have demonstrated its ability to inhibit cancer cell growth, improving its
795 physicochemical characteristics is essential to maximize its therapeutic potential in *in vivo*
796 evaluation. Nanotechnology-based drug delivery systems have emerged as an effective strategy
797 to overcome many limitations by increasing drug bioavailability, enhancing targeted delivery,
798 reducing the required dosage, minimizing adverse effects, and improving overall treatment
799 outcomes [59]. To enhance its anticancer activity, RTN has been incorporated into a polymer
800 (polysaccharide), thereby improving its bioavailability at the target site and its cytotoxicity
801 against SKOV-3 ovarian cancer cells. Similarly, several RTN-loaded nanoparticle
802 formulations have been designed to enhance stability, bioavailability, and therapeutic efficacy,
803 highlighting their potential for cancer treatment.

804 In the present study, RTN was incorporated into chitosan to form chitosan nanoparticles
805 via ionic gelation. The resulting nanoparticles were then coated with guar gum to produce

RTN-loaded chitosan/guar gum nanoparticles (RTN-CS/GG-NPs). Chitosan was used as the ideal carrier material because of its excellent biocompatibility, biodegradability, low toxicity, and ability to improve drug delivery. Chitosan-based nanoparticles can achieve controlled, targeted drug release, enhance drug stability, and promote greater accumulation of therapeutic agents at tumour sites by responding to the tumor microenvironment [60]. These characteristics make them promising nanocarriers for enhancing the effectiveness of anticancer agents while reducing unwanted side effects. Further, guar gum-based nanoparticles have gained considerable attention as natural drug-delivery carriers because they are derived from the galactomannan polysaccharide. These nanoparticles are biocompatible, biodegradable, cost-effective, and suitable for pharmaceutical applications [61]. Guar gum-coated NPs serve as highly effective biopolymeric drug delivery systems that dramatically enhance therapeutic efficacy by preventing premature drug degradation, evading immune clearance, and selectively releasing payloads at targeted physiological sites. Guar gum possesses several physicochemical characteristics that make it an attractive natural polymer for the development of advanced nanomedicine systems. Its excellent biocompatibility, biodegradability, and gel-forming ability help address many of the limitations associated with conventional drug delivery platforms [62]. A previously reported study demonstrated that guar gum was combined with chitosan nanoparticles to develop a nanocomposite hydrogel containing 5-fluorouracil. The incorporation of guar gum enhanced both the mechanical strength and thermal stability of the hydrogel. Furthermore, the chitosan nanoparticles provided sustained drug release in the colorectal region, with release kinetics indicating non-Fickian (anomalous) transport. The resulting drug-loaded nanocomposite hydrogel also demonstrated greater cytotoxic activity against HT-29 colon cancer cells, suggesting its potential as an effective platform for targeted colorectal cancer therapy [63].

Particle size, surface charge, and shape are important properties of anticancer agents-loaded nanoparticles used in cancer therapy [64]. These features enable them to effectively reach tumor tissues, prolong circulation, and release therapeutic agents in a controlled, targeted manner, thereby improving treatment effectiveness while reducing unwanted side effects. In the present study, a high amount of RTN (86.71 ± 1.35%) was successfully encapsulated within chitosan nanoparticles, which were then surface-coated with guar gum to obtain RTN-CS/GG nanoparticles. The structural, morphological, and physicochemical characteristics of the formulated RTN-CS/GG-NPs were thoroughly evaluated using FTIR, XRD, FESEM, HRTEM, and XPS. The characterization results confirmed the successful formation of RTN-CS/GG nanoparticles with a semi-crystalline structure, spherical morphology, and an average particle size of approximately 42.76 nm. Particle size plays a critical role in nanomedicine, particularly in cancer therapy, as nanoparticles in the nanoscale range can preferentially accumulate in tumour tissues via the enhanced permeability and retention (EPR) effect [65]. In addition, spherical nanoparticles are more readily internalized by cancer cells because their symmetrical geometry facilitates membrane interaction and promotes uptake through endocytosis. Surface charge, represented by the zeta potential, is another important parameter that influences nanoparticle stability and cellular interactions. The RTN-CS/GG nanoparticles exhibited a positive zeta potential of +57.6 mV, indicating excellent colloidal stability and suggesting favourable interactions with biological membranes. Furthermore, the formulation remained stable under physiological conditions and across a range of buffer pH values, demonstrating its suitability for biomedical and drug-delivery applications. The *in vitro* release behaviour of RTN from RTN-CS/GG nanoparticles was evaluated at predetermined time intervals using phosphate and acetate buffer solutions with different pH values. The release profile showed an initial burst during the first 24 h, followed by a slower, sustained release phase, indicating potential for prolonged therapeutic activity. Among the tested conditions, the

855 highest amount of RTN was released in acetate buffer at pH 5.8, which simulates the mildly
856 acidic microenvironment commonly associated with tumor tissues. This pH-responsive release
857 behaviour suggests that the nanoparticles can preferentially release the drug under cancer-like
858 conditions [66]. The RTN-CS/GG-NPs formulation was designed to achieve prolonged
859 circulation, controlled drug release, selective accumulation at the tumour site, and effective
860 interaction with cancer cells while minimizing undesirable effects on healthy tissues.
861 Furthermore, network pharmacology, molecular docking and molecular dynamics simulation
862 studies were performed to predict a potential RTN-binding target for significant anti-ovarian
863 cancer activity. Using SwissTargetPrediction to identify RTN's human targets, network
864 pharmacology first examined the predicted targets and intersected them with genes associated
865 with ovarian cancer, as identified in GeneCards and DisGeNET. After that, KEGG and GO
866 enrichment analyses were performed using DAVID and ShinyGO, and protein–protein
867 interaction (PPI) analysis was performed using STRING and Cytoscape tools. Among the
868 kinase-centred signalling hubs identified by our investigations, ESR1 stood out as a crucial
869 node. With a score of –9.2 kcal/mol, the docking experiments positioned RTN competitively
870 within ESR1. Molecular dynamics simulation studies showed that the RTN-ESR1 complex
871 remained highly stable throughout the simulation period.

872 The cytotoxicity and biocompatibility of freshly prepared RTN-CS/GG-NPs were
873 evaluated using the MTT assay in ovarian cancer (SKOV-3) cells and normal mouse fibroblast
874 (L929) cells. The results were compared with free-RTN. RTN-CS/GG-NPs exhibited a
875 concentration- and time-dependent inhibitory effect on SKOV-3 cells, with IC_{50} values of 23.6
876 μg/mL at 24 h and 10.4 μg/mL at 48 h of treatment. In contrast, the RTN-CS/GG-NPs
877 formulation showed excellent compatibility with normal L929 cells. Even at a concentration
878 of 100 μg/mL, cell viability remained high (93.87 ± 0.64%) after 24 h of exposure, indicating
879 minimal toxicity toward healthy cells. Compared with the RTN-CS/GG-NPs formulation, free

RTN exhibited lower anticancer activity. Treatment with 100 μg/mL free RTN resulted in SKOV-3 cell viabilities of 39.55 ± 1.19% after 24 h and 37.14 ± 1.91% after 48 h. Under the same experimental conditions, RTN-CS/GG-NPs reduced cell viability to 25.67 ± 2.41% and 18.19 ± 1.09% after 24 h and 48 h, respectively. The enhanced cytotoxic effect of RTN-CS/GG-NPs is likely due to improved cellular uptake and sustained intracellular delivery of RTN via the chitosan/guar gum nanoparticle system, leading to greater inhibition of ovarian cancer cell growth. Similarly, doxorubicin-loaded carboxymethyl chitosan (CCS)–carboxyl-modified guar gum (CGG) hydrogels exhibited pronounced cytotoxic activity against MCF-7 breast cancer cells, causing approximately 81.10% cell death. These findings indicate that the CCS–CGG hydrogel system effectively enhances the anticancer activity of doxorubicin and supports its sustained release. Also, these CCS–CGG hydrogels loaded with anticancer agents exhibited pH-dependent release over 3 days, with an accelerated release rate at tumor-specific pH [67]. The induction of apoptosis is a crucial therapeutic approach to inhibit ovarian cancer cell proliferation and overcome resistance to conventional anticancer therapies [68]. Cancer cells can evade apoptosis through multiple molecular mechanisms, including the overexpression of antiapoptotic proteins and the loss or mutation of tumour suppressor genes [69]. These alterations contribute to resistance against chemotherapeutic and other cytotoxic treatments, allowing cancer cells to survive and proliferate. Because apoptosis is a major regulator of cell survival, restoring apoptotic signalling has become an important strategy in cancer therapy [70]. Growing evidence suggests that naturally derived bioactive compounds can induce apoptosis in cancer cells and therefore hold promise as anticancer agents [71]. Among the commonly used methods for evaluating apoptosis, dual staining with acridine orange (AO) and ethidium bromide (EB) is a simple, rapid, and reliable technique for detecting morphological changes associated with cell death. This fluorescence-based assay does not require cell fixation, thereby minimizing fixation-related artifacts while enabling clear discrimination between

viable, apoptotic, and necrotic cells. To further evaluate the apoptosis-inducing potential of the formulated RTN-CS/GG nanoparticles, an AO/EB dual-staining assay was performed. Fluorescence microscopic examination revealed characteristic apoptotic features in RTN-CS/GG NP-treated cells, including nuclear condensation and fragmentation, cell shrinkage, and membrane blebbing, confirming the induction of apoptotic cell death. Similarly, RTN-chitosan nanoconjugate induced a cell-cycle arrest at the DNA synthesis phase, followed by apoptotic cell death in triple-negative breast cancer cells, as evidenced by AO/EB and DAPI fluorescence microscopy [72].

To further investigate the mechanism underlying the anticancer activity of RTN-CS/GG nanoparticles, intracellular reactive oxygen species (ROS) generation and mitochondrial membrane potential ($\Delta\Psi m$) were evaluated after 24 h of treatment. The results demonstrated that RTN-CS/GG-NPs significantly increased intracellular ROS production while causing a marked loss of mitochondrial membrane potential, indicating mitochondrial dysfunction. Excessive ROS generation induces oxidative stress by damaging essential cellular components, including lipids, proteins, nucleic acids, and intracellular organelles. Such oxidative damage can disrupt mitochondrial function and trigger apoptosis through the intrinsic signaling pathway [73]. Mitochondrial impairment promotes the release of cytochrome c into the cytosol, where it associates with apoptotic protease-activating factor-1 (Apaf-1) to form the apoptosome. This complex subsequently activates caspase-9, followed by caspase-3, ultimately leading to the execution of programmed cell death [74]. In addition, nuclear morphological changes associated with apoptosis were examined using 4′,6-diamidino-2-phenylindole (DAPI) staining. Fluorescence microscopy revealed nuclear condensation and fragmentation, providing further evidence that RTN-CS/GG-NPs induce apoptotic cell death through a mitochondria-mediated pathway.

5. Conclusion

The present study demonstrates the successful formulation of RTN-CS/GG-NPs using the ionic gelation approach. The formulated NPs exhibited improved anticancer activity against SKOV-3 ovarian cancer cells compared with free RTN, indicating that nanoparticle-based delivery enhanced RTN uptake and strengthened its therapeutic efficacy. The formulation strategy was designed to overcome the limitations of RTN's solubility by encapsulating it in nanosized particles, higher encapsulation efficiency, enhancing bioavailability, and facilitating delivery to cancer cells. To investigate the possible molecular targets and mechanism of action of RTN in ovarian cancer, a combination of network pharmacology, molecular docking, and molecular dynamics simulation approaches was applied. Computational analysis identified ESR1 as a potential target, exhibiting a strong binding interaction with RTN with a binding energy of −9.2 kcal/mol. The stable interaction between RTN and ESR1 was further confirmed through molecular dynamics analysis, which demonstrated consistent complex stability throughout the simulation period. These computational findings provide insights into potential molecular pathways underlying RTN-mediated anticancer activity and support the potential of RTN-CS/GG-NPs as a promising therapeutic delivery system for ovarian cancer treatment. The enhanced anticancer activity of RTN-CS/GG-NPs may be attributed to the efficient transport of encapsulated RTN into cancer cells through the synergistic properties of the polymeric delivery system. In this formulation, chitosan served as the primary nanoparticle-forming material, while guar gum was incorporated as a surface-coating polymer to enhance nanoparticle stability and functionality. The developed RTN-CS/GG-NPs exhibited high encapsulation efficiency (86.71 ± 1.35% w/w) and a drug-loading capacity of 9.88 ± 0.74% w/w. Furthermore, the in vitro release study revealed a sustained, controlled release profile of RTN from the nanoparticle matrix. The successful formation and physicochemical characteristics of RTN-CS/GG-NPs were confirmed using multiple analytical techniques, including FTIR, XRD, XPS, particle-size analysis, and FESEM. Biological evaluation

demonstrated that RTN-CS/GG-NPs effectively inhibited SKOV-3 ovarian cancer cell proliferation and induced apoptosis, potentially via RTN-mediated modulation of the ESR1 signalling pathway. However, this study has certain limitations, particularly the absence of *in vivo* biodistribution and pharmacokinetic assessments, which are necessary to determine the accumulation and bioavailability of RTN at the tumor site. Further preclinical investigations are required to validate the therapeutic potential of this nanocarrier system. Nevertheless, the current findings suggest that RTN-CS/GG-NPs represent a promising platform for the development of targeted therapeutic strategies against ovarian cancer and other cancer types.

Data availability

No data was used for the research described in the article.

Acknowledgments

We would like to thank and gratefully acknowledge the grants from NSTC to A. Santhana Krishna Kumar (NSTC 114-2221-E-110-007; NSTC 115-2221-E-110-052) for the financial support of this study, and NSYSU-KMU Joint Research Project (NSYSU-KMU 115-P17) for the financial support of this study.

Funding

KS would like to thank SRMIST, Trichy, for their financial support, vide number SRM/IST-TRY/RI/007.

Contributions

Jeganpandi Senthamarai Pandi: Writing – original draft, Methodology, Investigation, Formal analysis, Data curation, Conceptualization. **Parasuraman Pavadai**: Writing – review & editing, Supervision, Methodology. **Murugesan Sankaranarayanan**: Writing – review & editing, Resources. **Pavithra Velmurugan**: Writing – review & editing, Resources. **Veni Subramanyam**: Writing – review & editing, Resources. **Yuan-Pin Chang**: Writing – review & editing, Resources, Project administration, Methodology, Conceptualization. **A. Santhana**

Krishna Kumar: Writing – review & editing, Resources, Project administration, Methodology, Conceptualization. **Selvaraj Kunjiappan**: Writing – review & editing, Supervision, Project administration, Methodology, Conceptualization.

Ethics declarations

Competing interests

The authors declare no competing interests.

Consent to participate

Not applicable. No human participants were involved in this study.

Consent to publish

Not applicable.

Ethics approval

Not applicable (there are no animals and human subjects in this study).

References

[1] C. Mattiuzzi, G. Lippi, Current cancer epidemiology, Journal of epidemiology and global health 9(4) (2019) 217-222.

[2] K. Sathishkumar, M. Chaturvedi, P. Das, S. Stephen, P. Mathur, Cancer incidence estimates for 2022 & projection for 2025: result from National Cancer Registry Programme, India, The Indian journal of medical research 156(4-5) (2023) 598.

[3] G. Sathish, L. Monavarshini, K. Sundaram, S. Subramanian, G. Kannayiram, Immunotherapy for lung cancer, Pathology-Research and Practice 254 (2024) 155104.

[4] M. Nieberler, U. Reuning, F. Reichart, J. Notni, H.-J. Wester, M. Schwaiger, M. Weinmüller, A. Räder, K. Steiger, H. Kessler, Exploring the role of RGD-recognizing integrins in cancer, Cancers 9(9) (2017) 116.

[5] K.M. Coyle, J.E. Boudreau, P. Marcato, Genetic mutations and epigenetic modifications: driving cancer and informing precision medicine, BioMed research international 2017(1) (2017) 9620870.

[6] Z. Liu, J. Chen, Y. Ren, S. Liu, Y. Ba, A. Zuo, P. Luo, Q. Cheng, H. Xu, X. Han, Multi-stage mechanisms of tumor metastasis and therapeutic strategies, Signal transduction and targeted therapy 9(1) (2024) 270.

[7] A. Mazidimoradi, Z. Momenimovahed, L. Allahqoli, A. Tiznobaik, N. Hajinasab, H. Salehiniya, I. Alkatout, The global, regional and national epidemiology, incidence, mortality, and burden of ovarian cancer, Health Science Reports 5(6) (2022) e936.

[8] A.M. Karst, R. Drapkin, Ovarian cancer pathogenesis: a model in evolution, Journal of oncology 2010(1) (2010) 932371.

[9] N.N. Adjei, P.G. Yeh, A. Haas, C.C. Sun, H. Zhao, R. Stone, K.L. Roche, K.H. Lu, I. Toumazis, L.A. Meyer, Opportunistic salpingectomy during gynecologic and non-gynecologic abdominopelvic procedures for ovarian cancer primary prevention: a cost-effectiveness analysis, International Journal of Gynecological Cancer (2025) 102884.

[10] U.A. Matulonis, A.K. Sood, L. Fallowfield, B.E. Howitt, J. Sehouli, B.Y. Karlan, Ovarian cancer, Nature reviews Disease primers 2(1) (2016) 16061.

[11] J. Prat, Ovarian carcinomas: five distinct diseases with different origins, genetic alterations, and clinicopathological features, Virchows Archiv 460(3) (2012) 237-249.

[12] B. Goff, Symptoms associated with ovarian cancer, Clinical obstetrics and gynecology 55(1) (2012) 36-42.

[13] B.M. Reid, J.B. Permuth, T.A. Sellers, Epidemiology of ovarian cancer: a review, Cancer biology & medicine 14(1) (2017) 9-32.

[14] S.A. Sahu, D. Shrivastava, A comprehensive review of screening methods for ovarian masses: towards earlier detection, Cureus 15(11) (2023).

[15] A. Chandra, C. Pius, M. Nabeel, M. Nair, J.K. Vishwanatha, S. Ahmad, R. Basha, Ovarian cancer: Current status and strategies for improving therapeutic outcomes, Cancer medicine 8(16) (2019) 7018-7031.

[16] B.T. Hennessy, R.L. Coleman, M. Markman, Ovarian cancer, The lancet 374(9698) (2009) 1371-1382.

[17] F.U. Vaidya, A. Sufiyan Chhipa, V. Mishra, V.K. Gupta, S.G. Rawat, A. Kumar, C. Pathak, Molecular and cellular paradigms of multidrug resistance in cancer, Cancer reports 5(12) (2022) e1291.

[18] J.S. Pandi, P. Pavadai, T. Panneerselvam, M. Sankaranarayanan, S. Kunjiappan, Enhanced anticancer activity of naringenin-encapsulated poly (lactic acid)/neem gum nanoparticles for breast cancer cells, Biomedical Materials 21(1) (2026) 015017.

[19] C.A. Dehelean, I. Marcovici, C. Soica, M. Mioc, D. Coricovac, S. Iurciuc, O.M. Cretu, I. Pinzaru, Plant-derived anticancer compounds as new perspectives in drug discovery and alternative therapy, Molecules 26(4) (2021) 1109.

[20] W. Sun, M.H. Shahrajabian, Therapeutic potential of phenolic compounds in medicinal plants—Natural health products for human health, Molecules 28(4) (2023) 1845.

[21] M. Iriti, E.M. Varoni, S. Vitalini, Bioactive Compounds in Health and Disease–Focus on Rutin, Bioactive Compounds in Health and Disease-Online ISSN: 2574-0334 6(10) (2023) 235-242.

[22] J.M. Al-Khayri, G.R. Sahana, P. Nagella, B.V. Joseph, F.M. Alessa, M.Q. Al-Mssallem, Flavonoids as potential anti-inflammatory molecules: a review, Molecules 27(9) (2022) 2901.

[23] A. Ghorbani, Mechanisms of antidiabetic effects of flavonoid rutin, Biomedicine & Pharmacotherapy 96 (2017) 305-312.

1051 [24] W. Wang, Q.-H. Wu, Y. Sui, Y. Wang, X. Qiu, Rutin protects endothelial dysfunction by
1052 disturbing Nox4 and ROS-sensitive NLRP3 inflammasome, Biomedicine & Pharmacotherapy
1053 86 (2017) 32-40.
1054 [25] A.B. Enogieru, W. Haylett, D.C. Hiss, S. Bardien, O.E. Ekpo, Rutin as a potent
1055 antioxidant: Implications for neurodegenerative disorders, Oxidative medicine and cellular
1056 longevity 2018(1) (2018) 6241017.
1057 [26] Z. Calis, R. Mogulkoc, A.K. Baltaci, The roles of flavonols/flavonoids in
1058 neurodegeneration and neuroinflammation, Mini Reviews in Medicinal Chemistry 20(15)
1059 (2020) 1475-1488.
1060 [27] Z. Nouri, S. Fakhri, K. Nouri, C.E. Wallace, M.H. Farzaei, A. Bishayee, Targeting
1061 multiple signaling pathways in cancer: The rutin therapeutic approach, Cancers 12(8) (2020)
1062 2276.
1063 [28] S. Sharma, A. Ali, J. Ali, J.K. Sahni, S. Baboota, Rutin: therapeutic potential and recent
1064 advances in drug delivery, Expert opinion on investigational drugs 22(8) (2013) 1063-1079.
1065 [29] Y. Yao, Y. Zhou, L. Liu, Y. Xu, Q. Chen, Y. Wang, S. Wu, Y. Deng, J. Zhang, A. Shao,
1066 Nanoparticle-based drug delivery in cancer therapy and its role in overcoming drug resistance,
1067 Frontiers in molecular biosciences 7 (2020) 193.
1068 [30] J.K. Tee, L.X. Yip, E.S. Tan, S. Santitewagun, A. Prasath, P.C. Ke, H.K. Ho, D.T. Leong,
1069 Nanoparticles' interactions with vasculature in diseases, Chemical Society Reviews 48(21)
1070 (2019) 5381-5407.
1071 [31] L. Zhang, A.F. Radovic-Moreno, F. Alexis, F.X. Gu, P.A. Basto, V. Bagalkot, S. Jon, R.S.
1072 Langer, O.C. Farokhzad, Co-delivery of hydrophobic and hydrophilic drugs from
1073 nanoparticle–aptamer bioconjugates, ChemMedChem: Chemistry Enabling Drug Discovery
1074 2(9) (2007) 1268-1271.

[32] A.A. Yetisgin, S. Cetinel, M. Zuvin, A. Kosar, O. Kutlu, Therapeutic nanoparticles and their targeted delivery applications, Molecules 25(9) (2020) 2193.

[33] N. Kamaly, B. Yameen, J. Wu, O.C. Farokhzad, Degradable controlled-release polymers and polymeric nanoparticles: mechanisms of controlling drug release, Chemical reviews 116(4) (2016) 2602.

[34] R.N. Tharanathan, F.S. Kittur, Chitin—the undisputed biomolecule of great potential, (2003).

[35] N. Morin-Crini, E. Lichtfouse, G. Torri, G. Crini, Fundamentals and applications of chitosan, Sustainable agriculture reviews 35: chitin and chitosan: history, fundamentals and innovations, Springer2019, pp. 49-123.

[36] S. Tahmouzi, H. Meftahizadeh, S. Eyshi, A. Mahmoudzadeh, B. Alizadeh, N. Mollakhalili-Meybodi, M. Hatami, Application of guar (Cyamopsis tetragonoloba L.) gum in food technologies: A review of properties and mechanisms of action, Food Science & Nutrition 11(9) (2023) 4869-4897.

[37] R.R. Radwan, H.E. Ali, Radiation-synthesis of chitosan/poly (acrylic acid) nanogel for improving the antitumor potential of rutin in hepatocellular carcinoma, Drug delivery and translational research 11(1) (2021) 261-278.

[38] S.C. Gutiérrez-Ruíz, H. Cortes, M. González-Torres, Z.M. Almarhoon, E.S. Gürer, J. Sharifi-Rad, G. Leyva-Gómez, Optimize the parameters for the synthesis by the ionic gelation technique, purification, and freeze-drying of chitosan-sodium tripolyphosphate nanoparticles for biomedical purposes, Journal of Biological Engineering 18(1) (2024) 12.

[39] R.R. Rajeshkumar, P. Pavadai, T. Panneerselvam, S.R.K. Pandian, A.S.K. Kumar, P. Maszczyk, E. Babkiewicz, S.J. Kabilan, S. Kunjiappan, Enhanced delivery of retinoic acid to breast cancer cells by folate receptor-targeted folic acid-conjugated glutenin nanoparticles for

promising treatment of breast cancer, Journal of Polymers and the Environment 32(5) (2024) 2120-2139.

[40] P. Petchimuthu, S. Kunjiappan, S.R.K. Pandian, M. Sankaranarayanan, K. Sundar, Sorghum grain-derived Kafirin nanoparticles for effective delivery of corosolic acid into breast cancer cells for potential treatment of breast cancer, Journal of Cluster Science 36(3) (2025) 81.

[41] S.R.K. Pandian, P. Pavadai, S. Vellaisamy, V. Ravishankar, P. Palanisamy, L.M. Sundar, V. Chandramohan, M. Sankaranarayanan, T. Panneerselvam, S. Kunjiappan, Formulation and evaluation of rutin-loaded solid lipid nanoparticles for the treatment of brain tumor, Naunyn-Schmiedeberg's Archives of Pharmacology 394(4) (2021) 735-749.

[42] E. Pandi, B.F. Proskhan, S. Kunjiappan, K. Sundar, V. Balakrishnan, Fabrication, characterization and evaluation of gallic acid-encapsulated Curdlan gum nanoparticles with potential application for breast cancer treatment, Journal of Polymers and the Environment 32(7) (2024) 3071-3088.

[43] B.S. Kumar, B.G.H. Dinesh, S. Ganjipete, M. Ramar, S. Murugesan, D.N. Ammunje, S. Kunjiappan, P. Pavadai, Therapeutic Potential of Morin in Alzheimer's Disease: An Integrated Network Pharmacology, Molecular Docking, ADMET, and Molecular Dynamics Study, ChemistrySelect 11(7) (2026) e06777.

[44] C.-H. Chin, S.-H. Chen, H.-H. Wu, C.-W. Ho, M.-T. Ko, C.-Y. Lin, cytoHubba: identifying hub objects and sub-networks from complex interactome, BMC systems biology 8(Suppl 4) (2014) S11.

[45] T. Wang, Z. Shao, Y. Xiao, X. Zhang, Y. Chen, B. Shi, S. Chen, Y. Wang, J. Peng, X. Shang, Predicting hepatoma-related genes based on representation learning of PPI network and gene ontology annotations, 2021 IEEE International Conference on Bioinformatics and Biomedicine (BIBM), IEEE, 2021, pp. 1892-1898.

[46] K. Rasool, A. Bhatti, A.M. Satti, R.Z. Paracha, P. John, Computational insights into the inhibitory mechanism of type 2 diabetes mellitus by bioactive components of Oryza sativa L. indica (black rice), Frontiers in pharmacology 15 (2024) 1457383.

[47] J. Xu, Y. Yang, Integrated gene expression profiling analysis reveals potential molecular mechanisms and candidate biomarkers for early risk stratification and prediction of STEMI and post-STEMI heart failure patients, Frontiers in Cardiovascular Medicine 8 (2021) 736497.

[48] S. Fu, Y. Zhou, C. Hu, Z. Xu, J. Hou, Network pharmacology and molecular docking technology-based predictive study of the active ingredients and potential targets of rhubarb for the treatment of diabetic nephropathy, BMC complementary medicine and therapies 22(1) (2022) 210.

[49] A. Khan, S. Ganjipete, P. Kumar Seetharaman, C. Selvaraj, S. Kunjiappan, A.R. Mahesh, P.S. Rajinikanth, D. Desai, D.N. Ammunje, P. Pavadai, Deciphering the Multi-Target Anticancer Potential of β-Sitosterol in Breast Cancer Through Integrated Computational Approaches, Computational Biology and Chemistry (2026) 109257.

[50] S. Kunjiappan, M. Sankaranarayanan, P. Parasuraman, Sialic acid-receptor targeted Epirubicin and Naringin-loaded sialic acid-conjugated silk fibroin nanoparticles for enhanced lung cancer treatment, Journal of Polymers and the Environment 34(4) (2026) 92.

[51] J. Das, Y.-J. Choi, J.W. Han, A.M.M.T. Reza, J.-H. Kim, Nanoceria-mediated delivery of doxorubicin enhances the anti-tumour efficiency in ovarian cancer cells via apoptosis, Scientific reports 7(1) (2017) 9513.

[52] M. Jabir, U.I. Sahib, Z. Taqi, A. Taha, G. Sulaiman, S. Albukhaty, A. Al-Shammari, M. Alwahibi, D. Soliman, Y.H. Dewir, Linalool-loaded glutathione-modified gold nanoparticles conjugated with CALNN peptide as apoptosis inducer and NF-κB translocation inhibitor in SKOV-3 cell line, International Journal of Nanomedicine (2020) 9025-9047.

[53] E. Piktel, I. Ościłowska, Ł. Suprewicz, J. Depciuch, N. Marcińczyk, E. Chabielska, P. Wolak, T. Wollny, M. Janion, M. Parlinska-Wojtan, ROS-mediated apoptosis and autophagy in ovarian cancer cells treated with peanut-shaped gold nanoparticles, International journal of nanomedicine (2021) 1993-2011.

[54] E.T. Salim, O. Almukhtar, M.F. Rafeeq, K.H. Rasool, R.A. Ismail, G.M. Sulaiman, M.S. Jabir, S.A. Mahdi, S.F. Jawad, M.A. Fakhri, Innovative Synthesis of Au@ WO3 Core–Shell Nanoparticles via Laser Ablation: Insights into Their Pharmaceutical Properties for Biomedical Applications, Plasmonics 20(6) (2025) 3817-3829.

[55] S. Masoumi, S.A. Aleyasin, S. Faghihi, miR-206-loaded albumin nanoparticles suppress ovarian cancer cells by inhibiting c-Met oncogenic pathway, Journal of Drug Delivery Science and Technology (2025) 107546.

[56] A. Al Hoque, S. Begum, D. Dutta, Occurrence, Chemical Nature, and Medicinal Benefits of Flavonoids-Rutin, Kaempferol, Quercetin, Anthocyanidins, Catechins, and Flavones, Dietary supplements and nutraceuticals, Springer2025, pp. 1-24.

[57] A.A. Perk, I. Shatynska-Mytsyk, Y.C. Gerçek, K. Boztaş, M. Yazgan, S. Fayyaz, A.A. Farooqi, Rutin mediated targeting of signaling machinery in cancer cells, Cancer cell international 14(1) (2014) 124.

[58] A.K. Farha, R.-Y. Gan, H.-B. Li, D.-T. Wu, A.G. Atanasov, K. Gul, J.-R. Zhang, Q.-Q. Yang, H. Corke, The anticancer potential of the dietary polyphenol rutin: Current status, challenges, and perspectives, Critical Reviews in Food Science and Nutrition 62(3) (2022) 832-859.

[59] A. Chowdhury, S. Kunjiappan, T. Panneerselvam, B. Somasundaram, C. Bhattacharjee, Nanotechnology and nanocarrier-based approaches on treatment of degenerative diseases, International nano letters 7(2) (2017) 91-122.

1172 [60] J. Li, C. Cai, J. Li, J. Li, J. Li, T. Sun, L. Wang, H. Wu, G. Yu, Chitosan-based
1173 nanomaterials for drug delivery, Molecules 23(10) (2018) 2661.
1174 [61] B. Mukherjee, L. Kumari, I. Ehsan, P. Ghosh, S. Banerjee, S. Chakraborty, M. Ray, A. Al
1175 Hoque, R. Sahoo, Guar gum-based nanomaterials in drug delivery and biomedical applications,
1176 Biopolymer-based nanomaterials in drug delivery and biomedical applications, Elsevier2021,
1177 pp. 143-164.
1178 [62] M. Sharahi, S.H. Bahrami, A. Karimi, A comprehensive review on guar gum and its
1179 modified biopolymers: Their potential applications in tissue engineering, Carbohydrate
1180 Polymers 347 (2025) 122739.
1181 [63] G. Dalei, D. Jena, S. Das, 5-Fluorouracil-loaded green chitosan nanoparticles/guar gum
1182 nanocomposite hydrogel in controlled drug delivery, Carbohydrate Research 545 (2024)
1183 109257.
1184 [64] J.-F. Hsu, S.-M. Chu, C.-C. Liao, C.-J. Wang, Y.-S. Wang, M.-Y. Lai, H.-C. Wang, H.-R.
1185 Huang, M.-H. Tsai, Nanotechnology and nanocarrier-based drug delivery as the potential
1186 therapeutic strategy for glioblastoma multiforme: An update, Cancers 13(2) (2021) 195.
1187 [65] K. Greish, Enhanced permeability and retention (EPR) effect for anticancer nanomedicine
1188 drug targeting, Cancer nanotechnology: Methods and protocols, Springer2010, pp. 25-37.
1189 [66] F. Erra Díaz, E. Dantas, J. Geffner, Unravelling the interplay between extracellular
1190 acidosis and immune cells, Mediators of inflammation 2018(1) (2018) 1218297.
1191 [67] S. Kanawade, A.H. Pandit, M. Nadeem, A. Gupta, Amide-Crosslinked Chitosan–Carboxy
1192 modified Guar Gum hydrogels for anticancer drug delivery, European Polymer Journal (2026)
1193 114987.
1194 [68] M. Binju, M.A. Amaya-Padilla, G. Wan, H. Gunosewoyo, Y. Suryo Rahmanto, Y. Yu,
1195 Therapeutic inducers of apoptosis in ovarian cancer, Cancers 11(11) (2019) 1786.

[69] R.S. Wong, Apoptosis in cancer: from pathogenesis to treatment, Journal of experimental & clinical cancer research 30(1) (2011) 87.

[70] E.V. Sazonova, M.A. Yapryntseva, N.V. Pervushin, R.I. Tsvetcov, B. Zhivotovsky, G.S. Kopeina, Cancer drug resistance: targeting proliferation or programmed cell death, Cells 13(5) (2024) 388.

[71] A. Naeem, P. Hu, M. Yang, J. Zhang, Y. Liu, W. Zhu, Q. Zheng, Natural products as anticancer agents: current status and future perspectives, Molecules 27(23) (2022) 8367.

[72] C. Chang, L. Zhang, Y. Miao, B. Fang, Z. Yang, Anticancer and Apoptotic-Inducing Effects of Rutin-Chitosan Nanoconjugates in Triple Negative Breast Cancer Cells: C. Chang et al, Journal of Cluster Science 32(2) (2021) 331-340.

[73] Y. Qin, C. Qian, W. Li, Q. Wang, Q. Sheng, Z. Chen, W. Zhang, W. Li, G. Ge, Z. Yan, Oxidative stress: Molecular mechanisms, diseases, and therapeutic targets, MedComm 7(2) (2026) e70600.

[74] C. Garrido, L. Galluzzi, M. Brunet, P. Puig, C. Didelot, G. Kroemer, Mechanisms of cytochrome c release from mitochondria, Cell Death & Differentiation 13(9) (2006) 1423-1433.

Figure Legends

Figure 1. Encapsulation efficiency of Rutin (RTN) into Chitosan NPs at various time points

Figure 2. RTN release from RTN-CS/GG-NPs in various buffer systems at time points. Data were presented as mean ± standard deviation (n = 3).

Figure 3. *In vitro* stability studies of RTN-CS/GG-NPs in various physiological solutions, buffers, saliva, and simulated gastric juice.

Figure 4. FTIR spectra of guar gum(a), RTN(b), chitosan(c) and RTN-CS/GG-NPs (d).

Figure 5. X-diffraction spectra of RTN(a), chitosan(b) and RTN-CS/GG-NPs(c); zeta potential of RTN-CS/GG-NPs (d), particle size analyzer of RTN-CS/GG-NPs(d), XPS spectrum of RTN-CS/GG-NPs(f).

Figure 6. FESEM images of RTN-CS/GG-NPs (a)-(c); HRTEM images of RTN-CS/GG-NPs (d)-(f).

Figure 7. Intersection targets of Rutin and Ovarian cancer (a), Targets of PPI network compounds against ovarian cancer. The STRING database's initial PPI data (b) showed the targets' intricate interconnections. Network analysis of targets with the highest rankings. (Top order, or very interactive is indicated by red; moderately interactive by orange; mildly interactive by yellow; and slightly interactive by blue.

Figure 8. 3D and 2D images of RTN with the top 11 proteins. 1SJ0-RTN complex (a)&(b), 3VW8-RTN (c)&(d), 4WMR-RTN (e)&(f), 5FXQ-RTN(g)& (h), 7JRA-RTN (i) &(j), 7KP9-RTN(k) &(l), 8F0W-RTN (m)&(n), 8F1X-RTN (o)&(p), 8K5W-RTN (q)&(r), 8W8K-RTN (s)&(t), and 8H78-RTN(u) &(v).

Figure 9. RMSD plot for 100 ns MD simulation of RTN-ESR1protein docked complex (a); RMSF plot of RTN for characterizing changes in the ligand atom positions (b); RTN-ESR1 protein contacts timeline representation (c); Percentage of amino acid and water-mediated interactions contribution in MD simulation with RTN (d), and RTN contacts with respect to the amino acids in the target protein ESR1 (e).

Figure 10. Assessment of cytotoxic and apoptotic effects of RTN-CS/GG-NPs on SKOV-3 cells. Cytotoxic activity of human ovarian cancer cells (SKOV-3) using different concentrations of RTN and RTN-CS/GG-NPs after 24 h and 48 h of treatment. The percentage of apoptotic cells increased in a dose-dependent manner. Morphology of the control cells (a), RTN-CS/GG-NPs treated cells (24 h) (b), and RTN-CS/GG-NPs treated cells (48 h) (c). Values are mean ± standard deviation of triplicate measurements (RTN-CS/GG-NPs) ($p < 0.05$)

(d). Morphology of the control cells (e), RTN-treated cells (24 h) (f), and RTN-treated cells (48 h) (g). Values are mean ± standard deviation of triplicate measurements (RTN-treated cells) ($p < 0.05$) (h). Cellular viability of L929 using different concentrations of RTN and RTN-CS/GG-NPs after 24 h of treatment. Morphology of the control cells (i), RTN-CS/GG-NPs-treated cells (24 h) (j), and RTN-treated cells (24 h) (k). Values are mean ± standard deviation of triplicate measurements ($p < 0.05$) (l). observed using a phase-contrast microscope.

Figure 11. Measurement of apoptotic morphological variation by double staining (AO/EtBr) control cells (untreated) (a), SKOV-3 cells treated with IC_{50} concentration of RTN-CS/GG-NPs (b) and RTN-treated cells(c) for 24 h. DAPI-stained images of SKOV-3 cancer cells. Control cells (d), treatment with RTN-CS/GG-NPs (e) and treatment with RTN (f). ROS generation was measured as relative fluorescence intensity using a fluorescence microscope; an image of untreated control cells was taken (g), and an increase in ROS was found in RTN-CS/GG-NPs-treated cells (h) and RTN-treated cells (i). Effects of RTN-CS/GG-NPs on mitochondrial transmembrane potential in MCF-7 cancer cells, control cells (untreated) (j), loss of mitochondrial transmembrane potential on treated RTN-CS/GG-NPs cells (k) and RTN-treated cells (l).

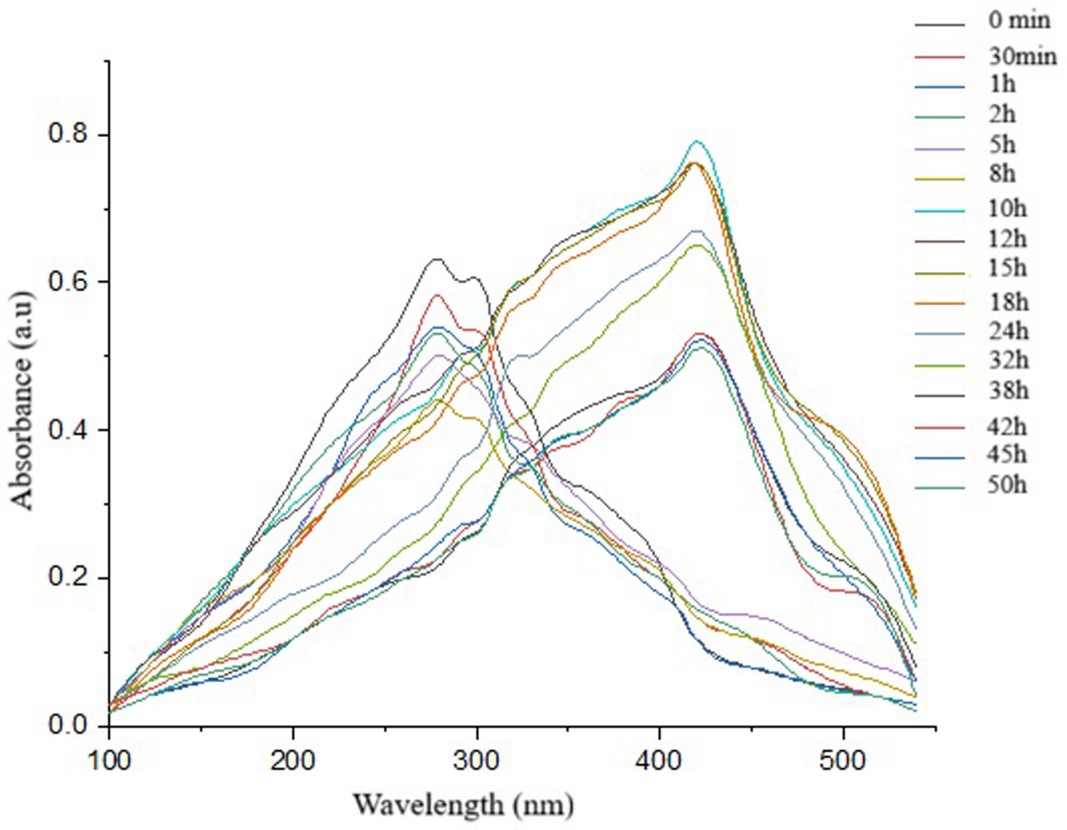
Figure 12. Cellular migration studies of ½ IC_{50} concentration of RTN-CS/GG-NPs (23.6µg/mL) and RTN (25.3 µg/mL). Control cells at 0 (a), 24 (b), and 48 (c) hours' time intervals, RTN-CS/GG-NPs treated cells at 0 (e), 24 (f), and 48 (g) hours' time intervals, and RTN treated cells at 0 (e), 24 (f), and 48 (g) hours' time intervals. Graph of wound closer are of untreated control (j), RTN-CS/GG-NPs treated cells (k) and RTN treated cells (l).

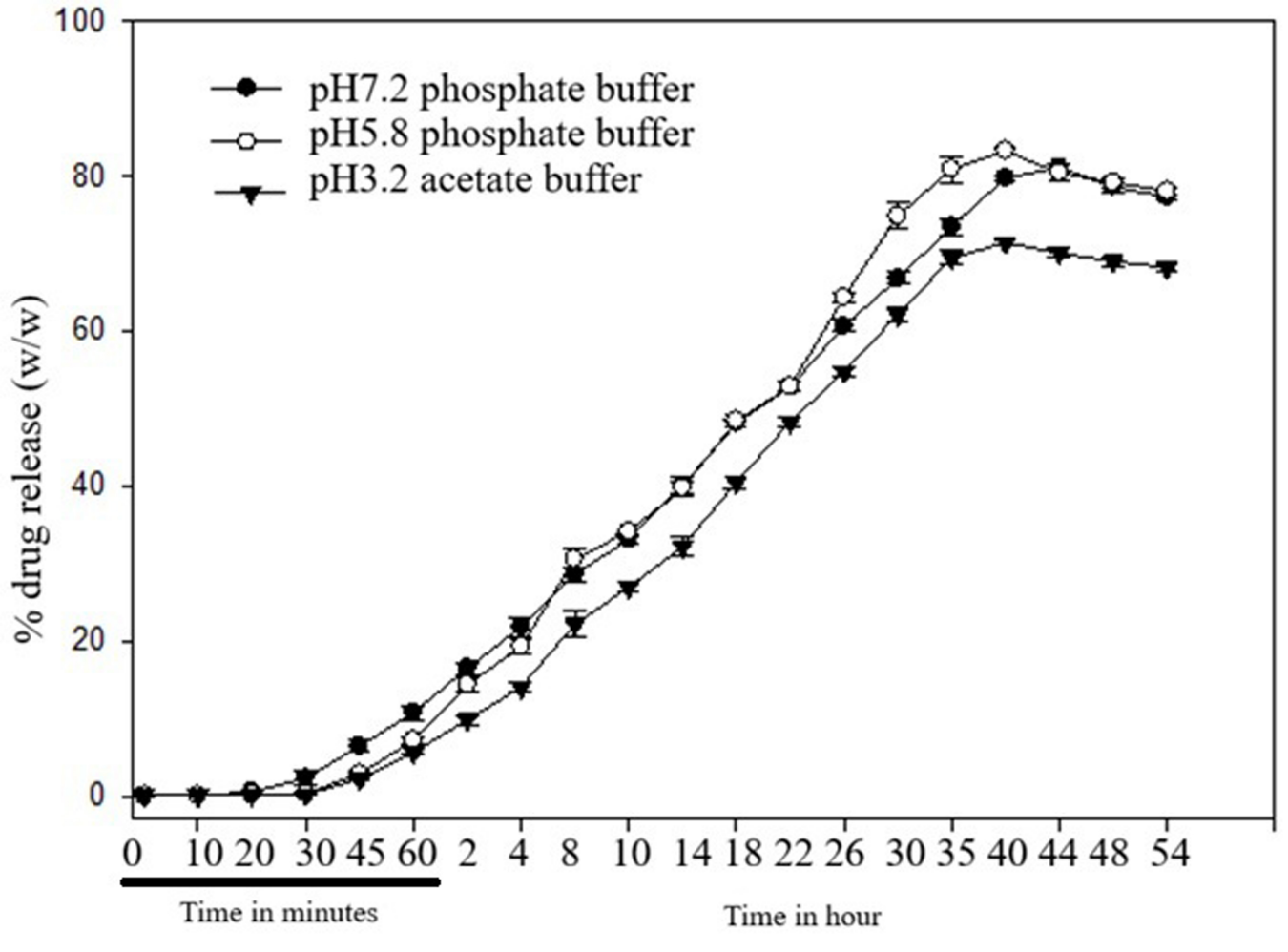
Table legends

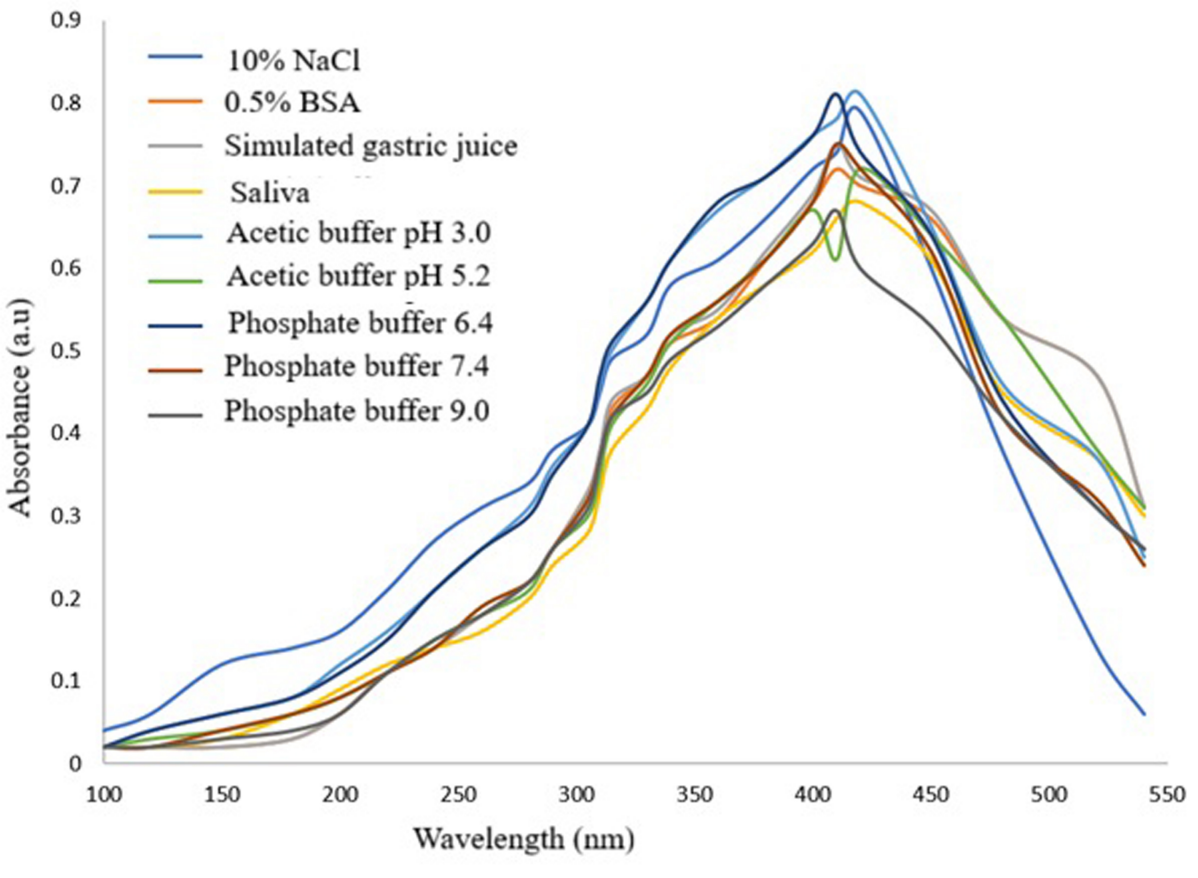
Table 1: Drug-release kinetics profile of Rutin from CS/GG NPs.
Where, AIC = Akaike information criterion, F = fraction of drug release in time t, K_0 =apparent rate constant of zero order release constant, K_1 = first order release constant, K_H =Higuchi constant, kKP =Korsmeyer-Peppas rate constant, kHC =Hixon-Crowell constant, kHB = Hopfenberg constant, n = diffusional exponent, and r^2 = Squared correlation coefficient.

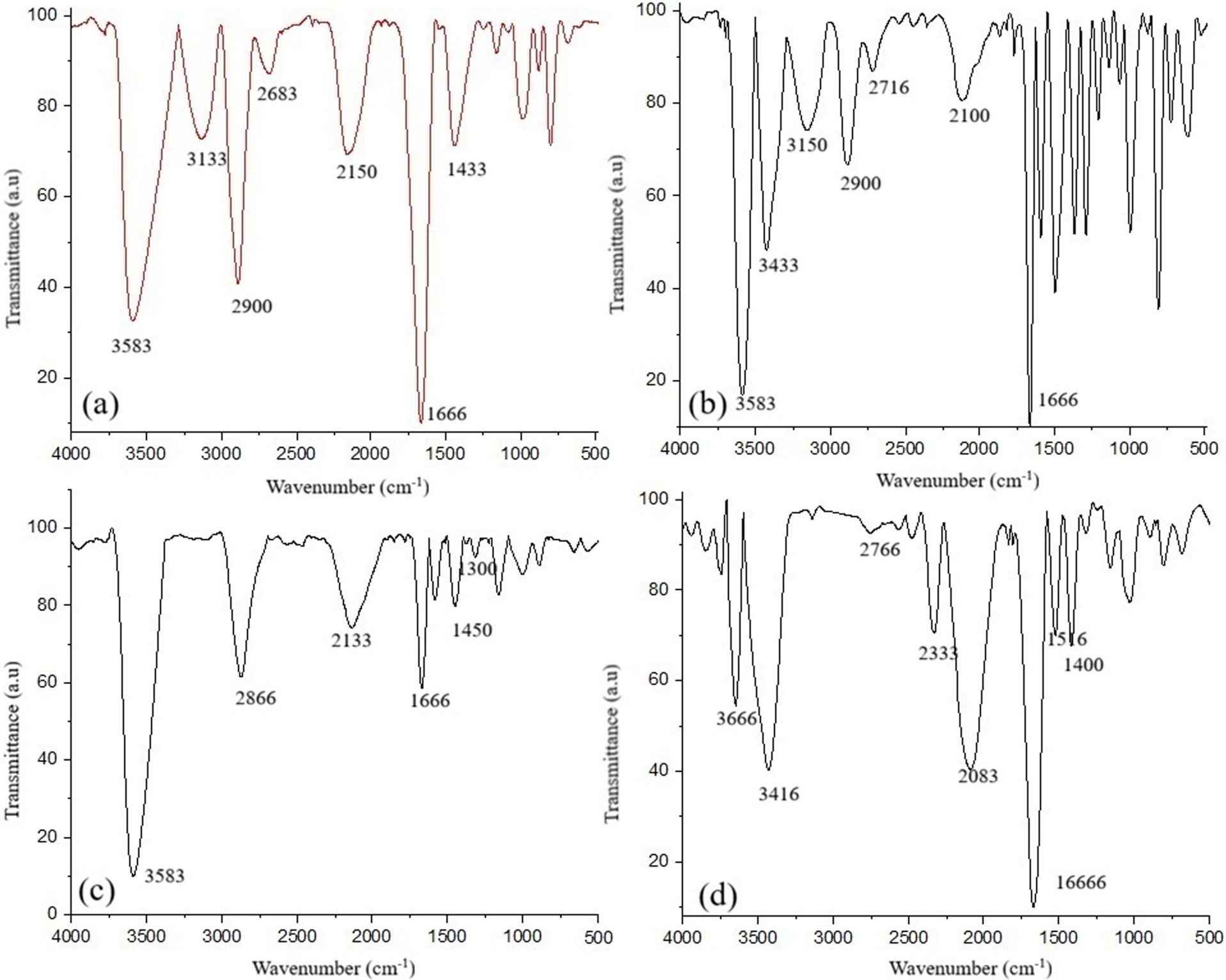
Figure 2. FTIR spectra of Guar gum, Rutin, Chitosan, and RTN-CS/GG NPs, along with their major peaks and corresponding functional groups.

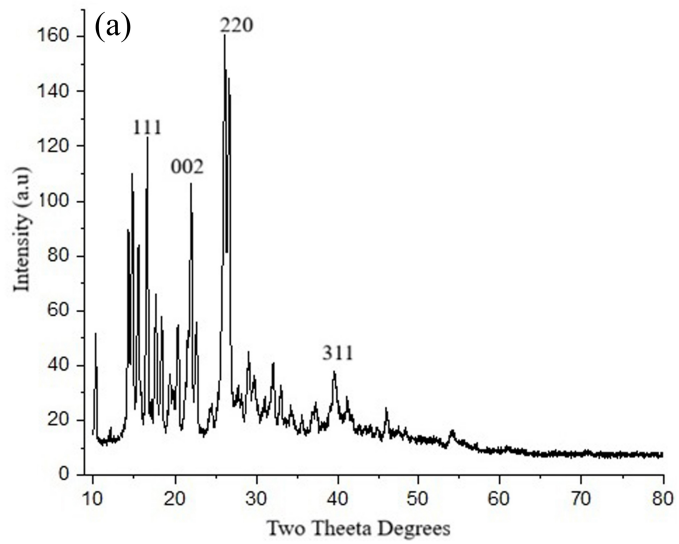
Table 3. Molecular docking results for Rutin against the top 11 proteins with Co-crystalized ligands.

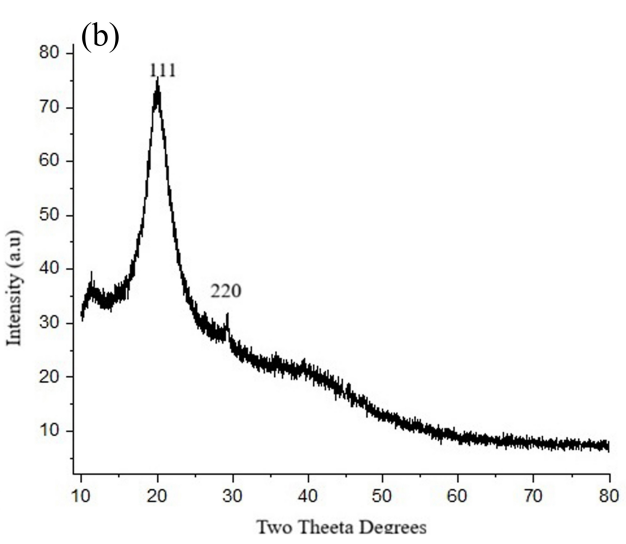

0 min
30min
1h
2h
5h
8h
10h
12h
15h
18h
24h
32h
38h
42h
45h
50h
Absorbance (a.u)
0.0
0.2
0.4
0.6
0.8
100
200
300
400
500
Wavelength (nm)

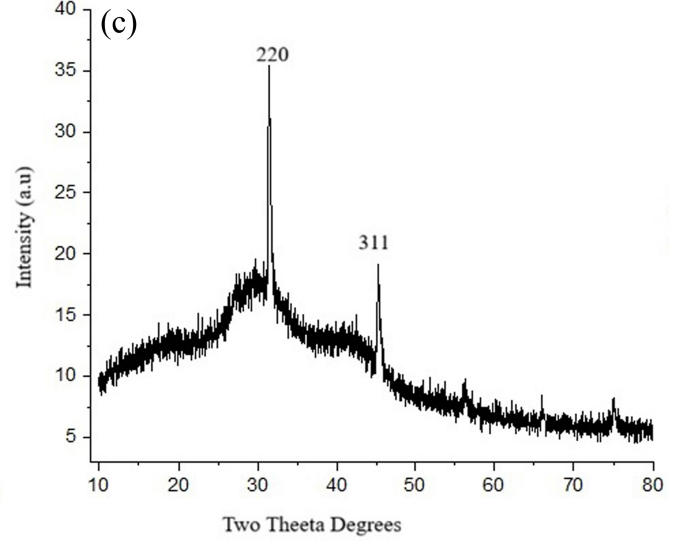

pH7.2 phosphate buffer
pH5.8 phosphate buffer
pH3.2 acetate buffer
% drug release (w/w)
100
80
60
40
20
0
0 10 20 30 45 60 2 4 8 10 14 18 22 26 30 35 40 44 48 54
Time in minutes
Time in hour

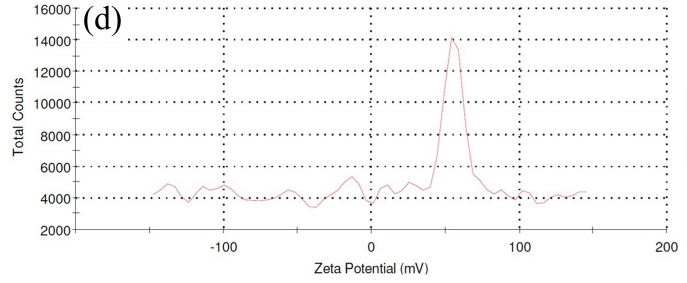

10% NaCl
0.5% BSA
Simulated gastric juice
Saliva
Acetic buffer pH 3.0
Acetic buffer pH 5.2
Phosphate buffer 6.4
Phosphate buffer 7.4
Phosphate buffer 9.0
Absorbance (a.u)
0.9
0.8
0.7
0.6
0.5
0.4
0.3
0.2
0.1
0
100
150
200
250
300
350
400
450
500
550
Wavelength (nm)

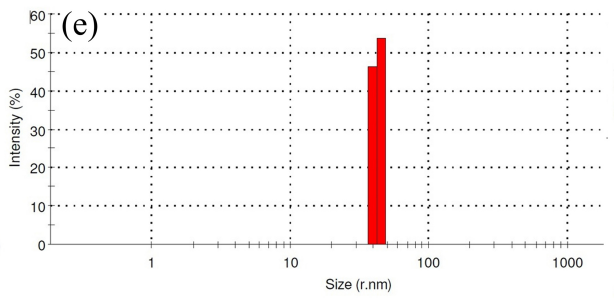

(a)
Transmittance (a.u)
Wavenumber (cm-1)
3583
3133
2900
2683
2150
1666
1433
(b)
3583
3433
3150
2900
2716
2100
1666
(c)
3583
2866
2133
1666
1450
1300
(d)
3666
3416
2766
2333
2083
1516
1400
16666

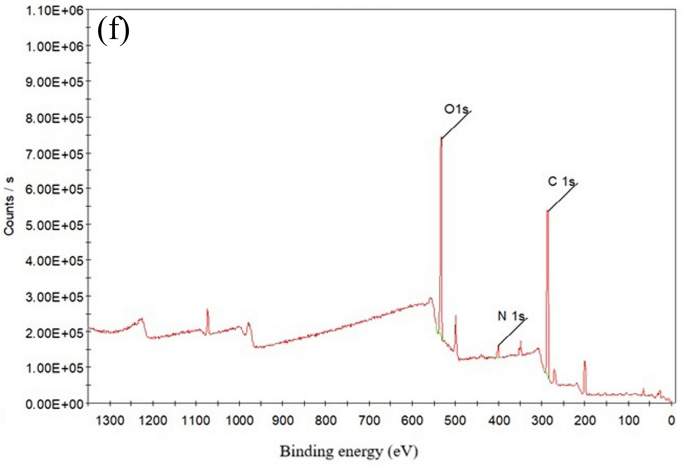

(a)
111
002
220
311
Intensity (a.u)
Two Theeta Degrees

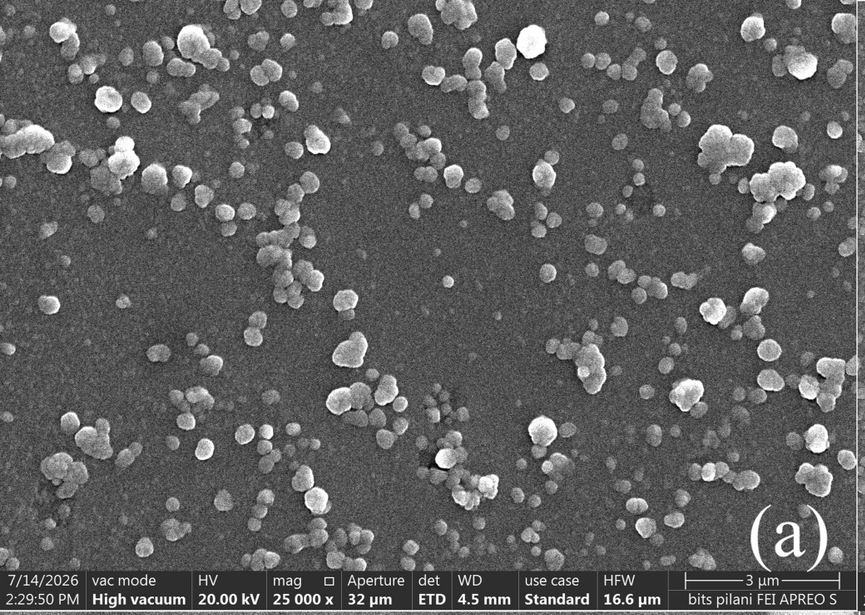

(b)
111
220
Intensity (a.u)
Two Theeta Degrees


(c)
220
311
Intensity (a.u)
Two Theeta Degrees

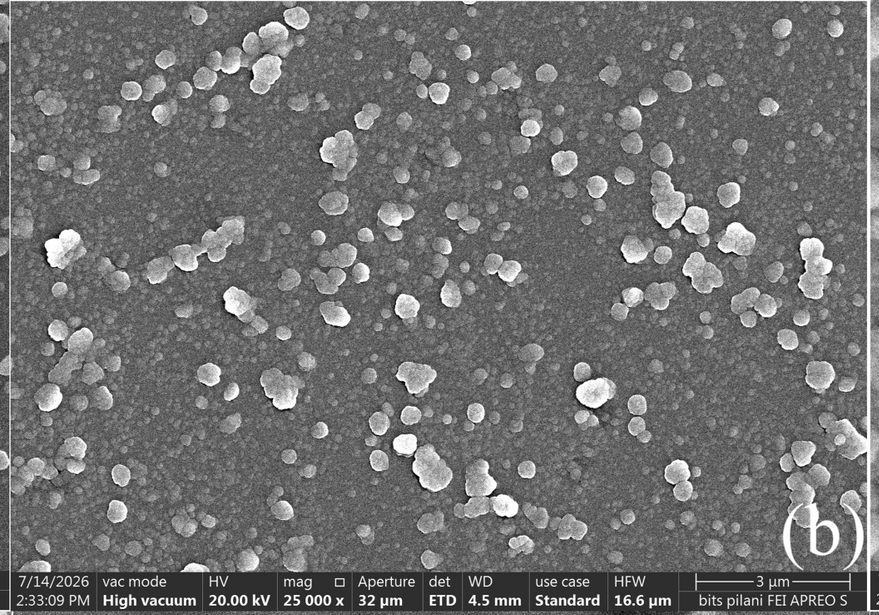

(d)
Total Counts
Zeta Potential (mV)


(e)
Intensity (%)
Size (r.nm)

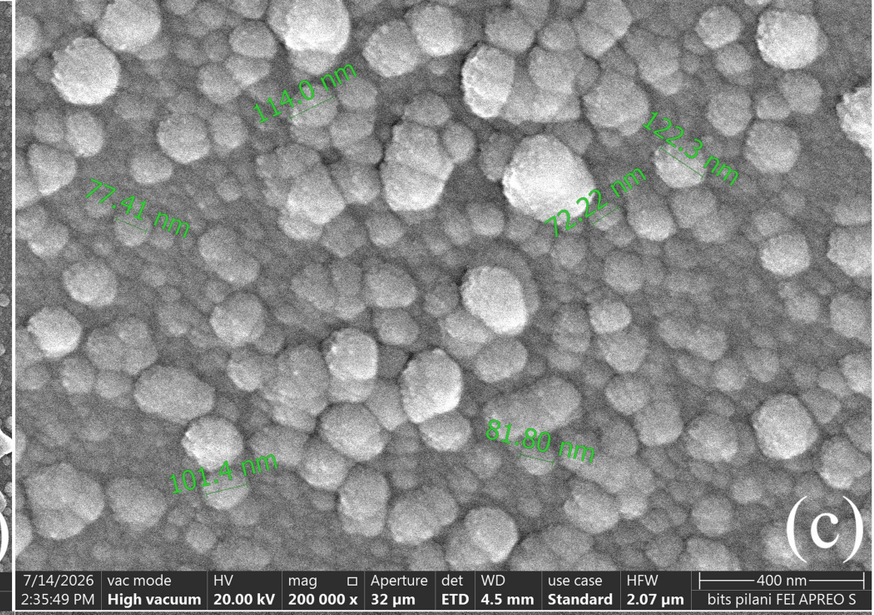

(f)
O1s
C 1s
N 1s
Counts / s
Binding energy (eV)



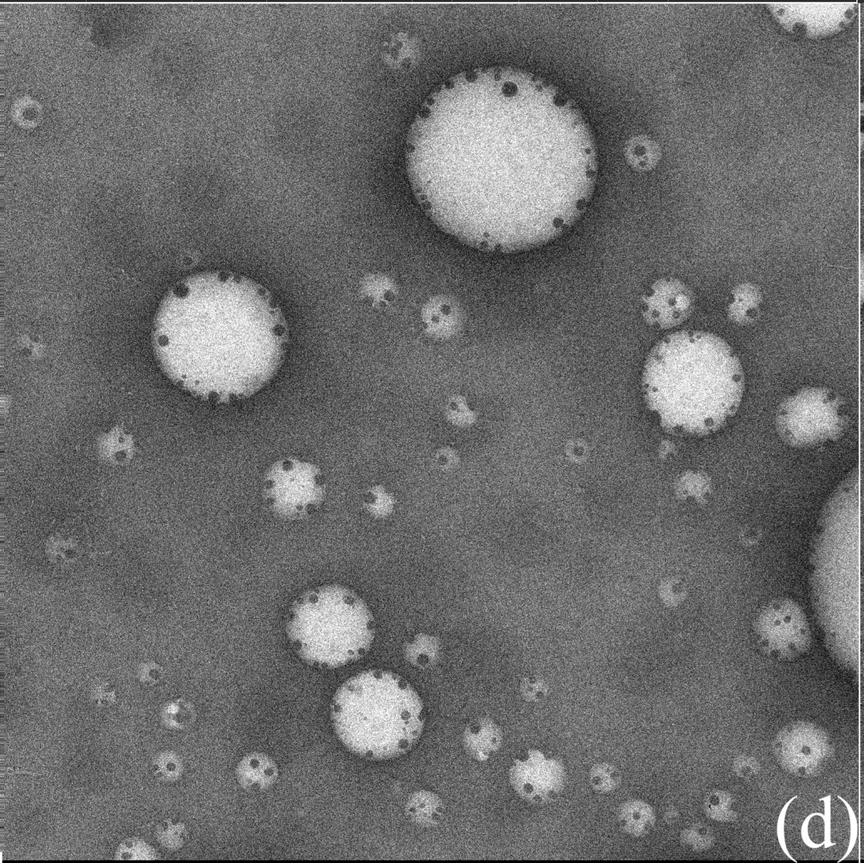
7/14/2026	vac mode	HV	mag	Aperture	det	WD	use case	HFW	3 µm
2:29:50 PM	**High vacuum**	**20.00 kV**	**25 000 x**	**32 µm**	**ETD**	**4.5 mm**	**Standard**	**16.6 µm**	bits pilani FEI APREO S

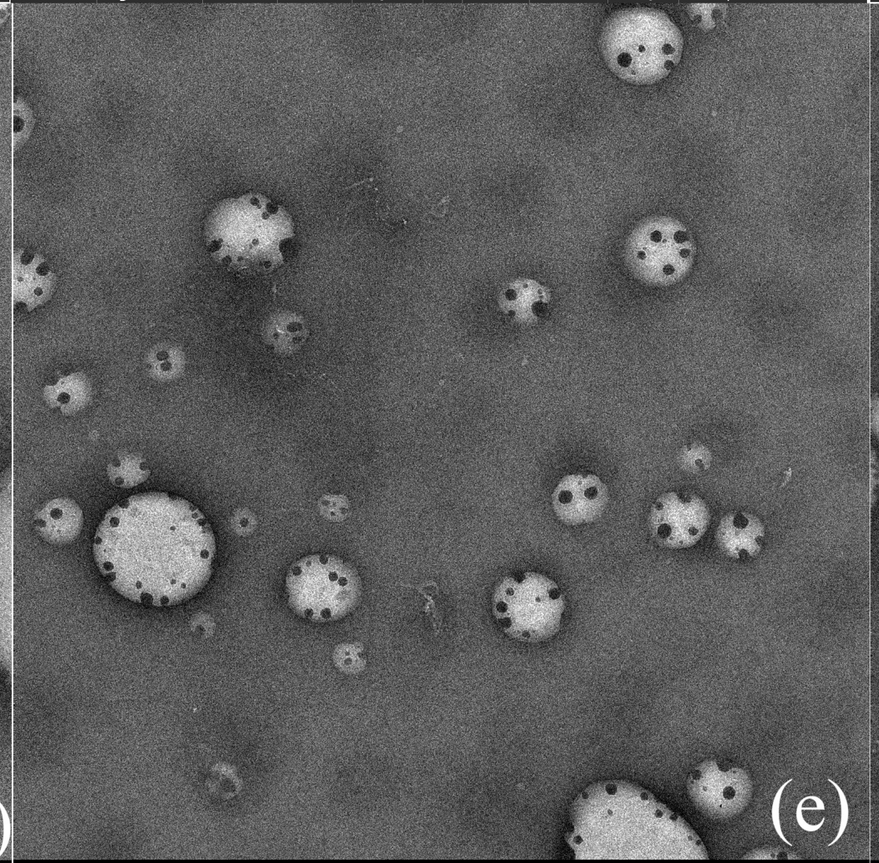


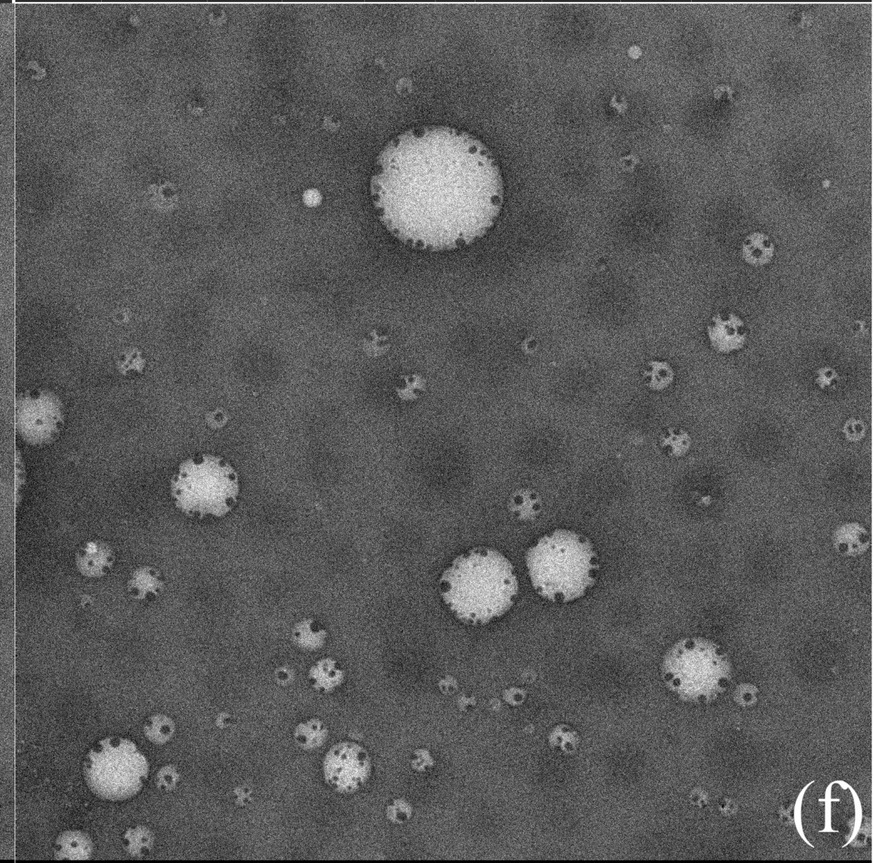
7/14/2026	vac mode	HV	mag	Aperture	det	WD	use case	HFW	3 µm
2:33:09 PM	**High vacuum**	**20.00 kV**	**25 000 x**	**32 µm**	**ETD**	**4.5 mm**	**Standard**	**16.6 µm**	bits pilani FEI APREO S



7/14/2026	vac mode	HV	mag	Aperture	det	WD	use case	HFW	400 nm
2:35:49 PM	**High vacuum**	**20.00 kV**	**200 000 x**	**32 µm**	**ETD**	**4.5 mm**	**Standard**	**2.07 µm**	bits pilani FEI APREO S



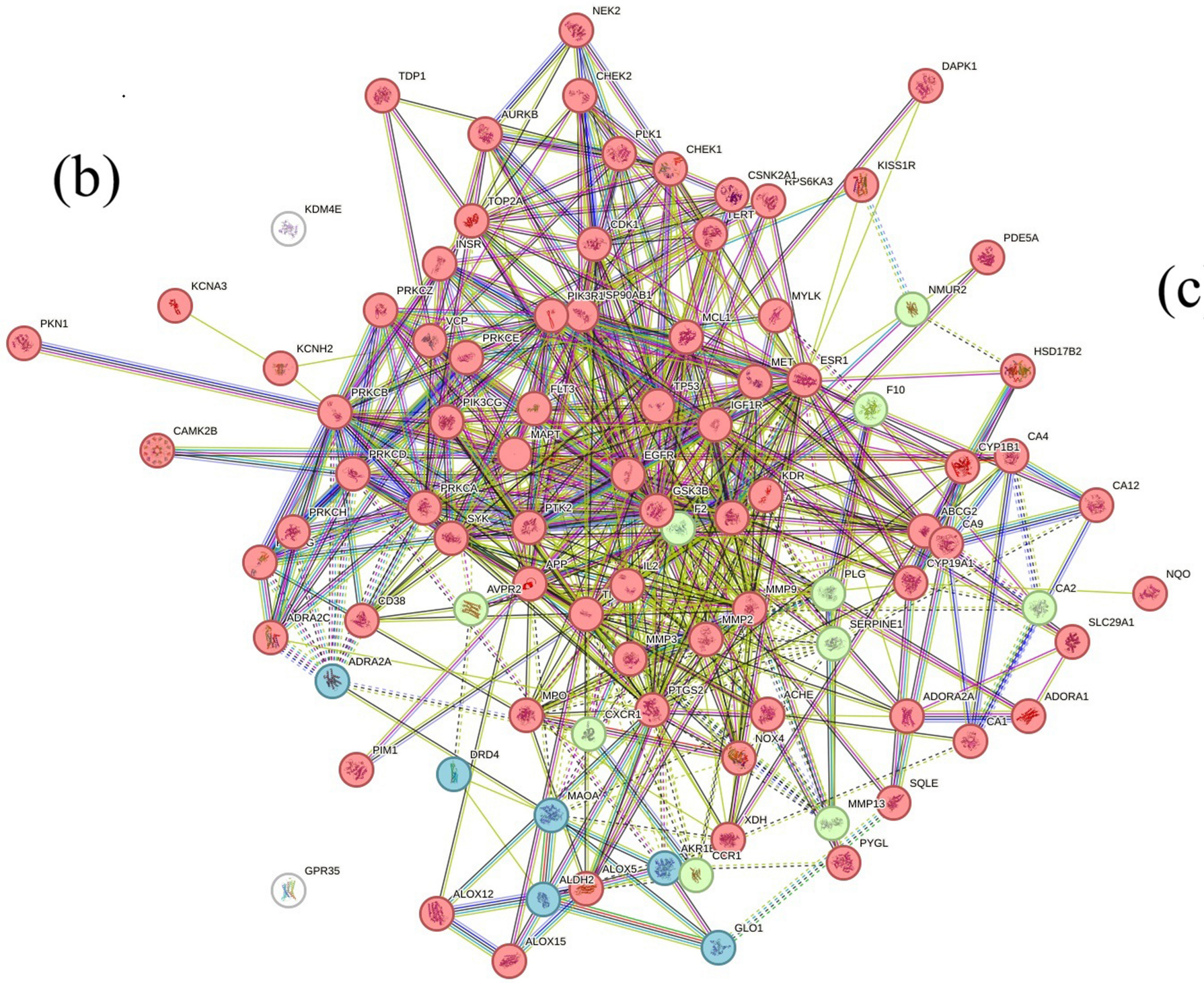




(a)


ligand-targets
(100)
disease-targets
(16812)
7
93
16719

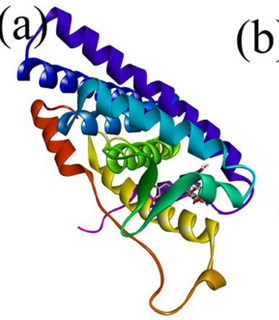
(b)


NEK2
TDP1
CHEK2
DAPK1
AURKB
PLK1
CHEK1
KISS1R
CSNK2A1
RPS6KA3
TOP2A
KDM4E
CDK1
TERT
INSR
PDE5A
KCNA3
PRKCZ
PIK3R1
HSP90AB1
MYLK
NMUR2
PKN1
VCP
MCL1
PRKCE
KCNH2
HSD17B2
MET
ESR1
PRKCB
FLT3
TP53
F10
PIK3CG
IGF1R
CAMK2B
MAPT
CA4
CYP1B1
PRKCD
EGFR
CA12
KDR
PRKCA
GSK3B
ABCG2
PRKCH
PTK2
F2
CA9
SYK
APP
IL2
CYP19A1
NQO
AVPR2
PLG
MMP9
CA2
CD38
TI
ADRA2C
MMP2
SERPINE1
SLC29A1
MMP3
ADRA2A
PTGS2
MPO
ACHE
ADORA2A
ADORA1
CXCR1
CA1
NOX4
PIM1
DRD4
SQLE
MAOA
MMP13
XDH
PYGL
AKR1B
CCR1
GPR35
ALOX5
ALDH2
ALOX12
GLO1
ALOX15

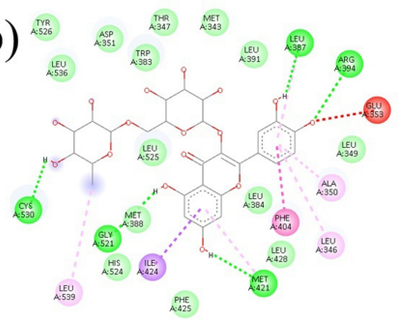
(c)


ESR1
HSP90AB1
MCL1
MMP9
EGFR
MET
MMP2
TNF
TP53
IGF1R

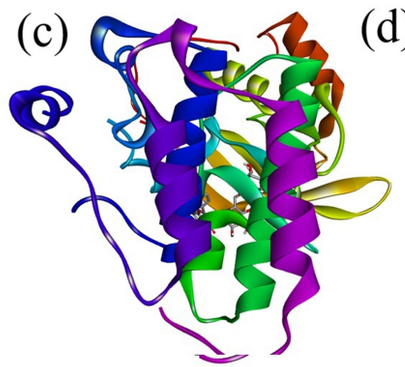
(a)



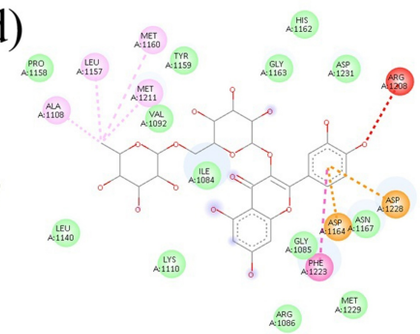
(b)



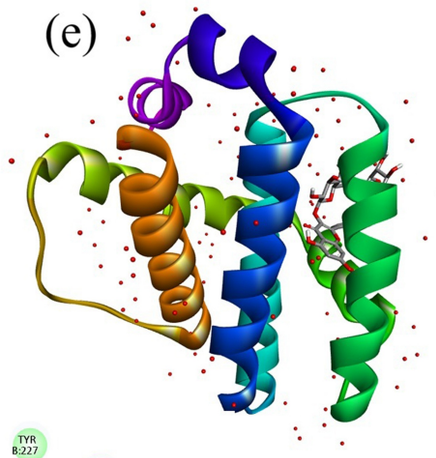
(c)



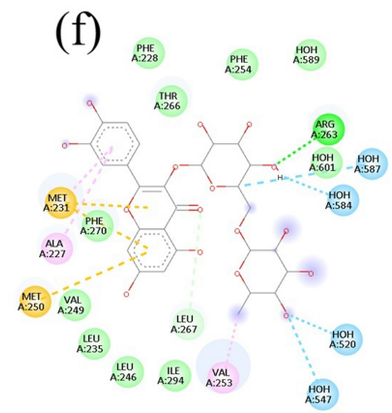
(d)



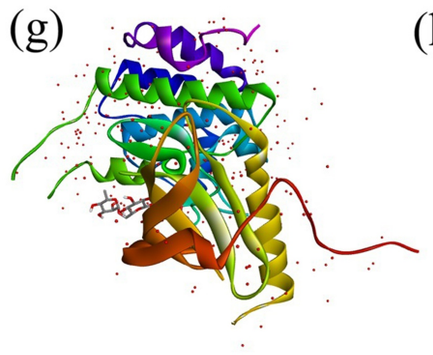
(e)



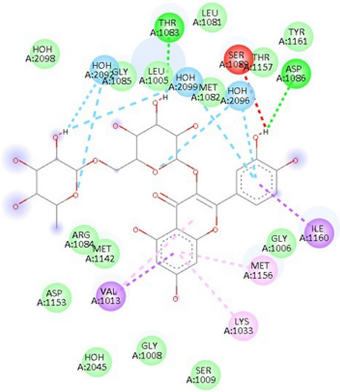
(f)



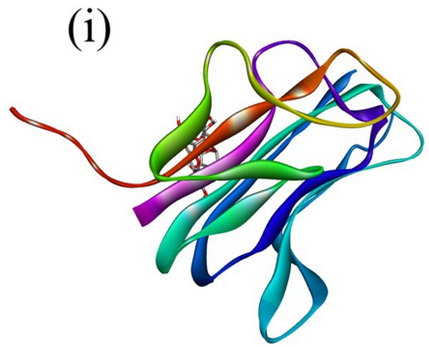
(g)



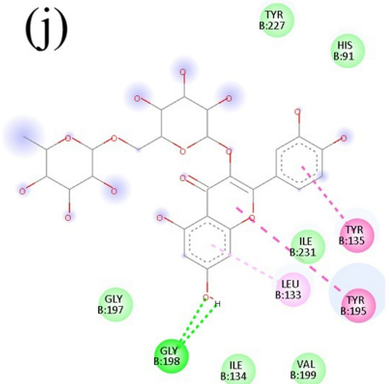
(h)



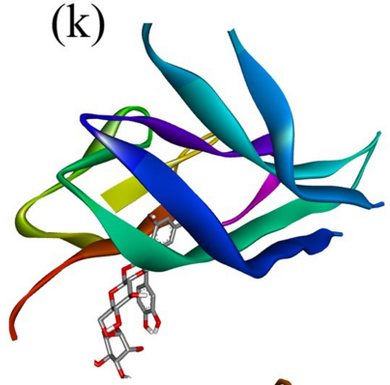
(i)



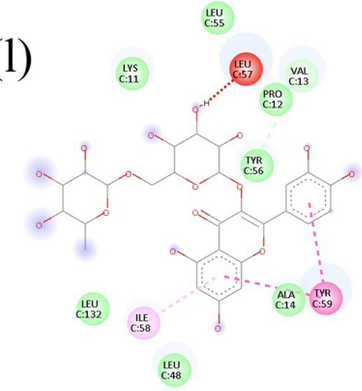
(j)



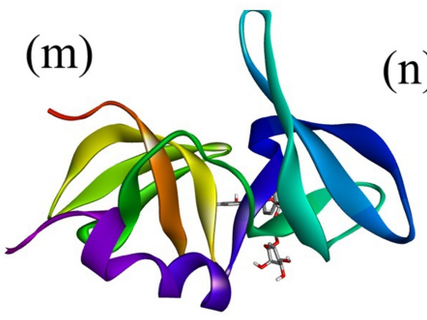
(k)



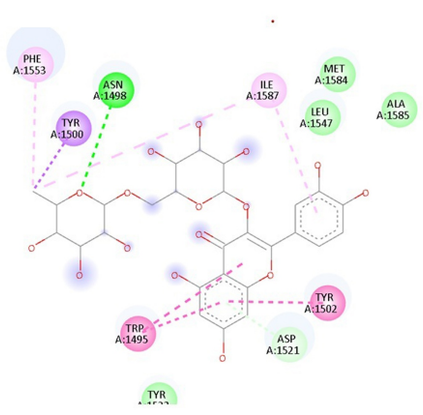
(l)



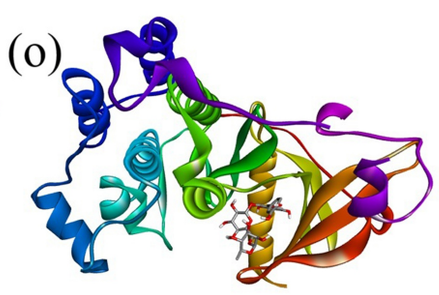
(m)



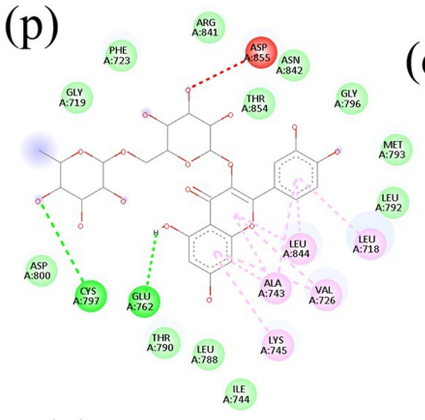
(n)



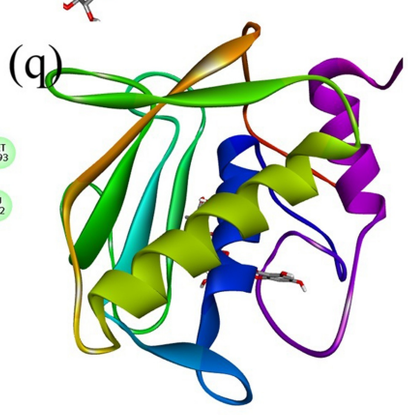
(o)



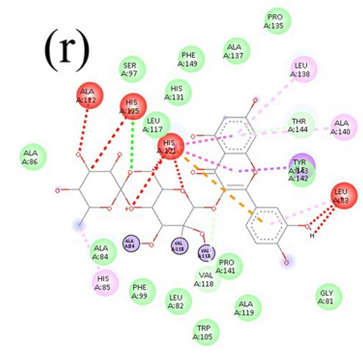
(p)



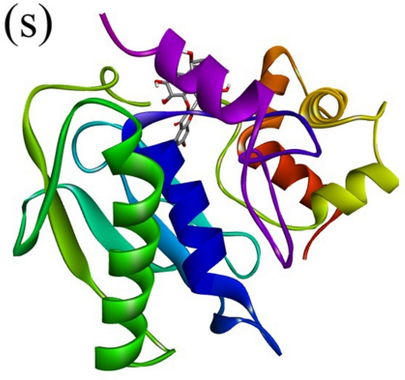
(q)



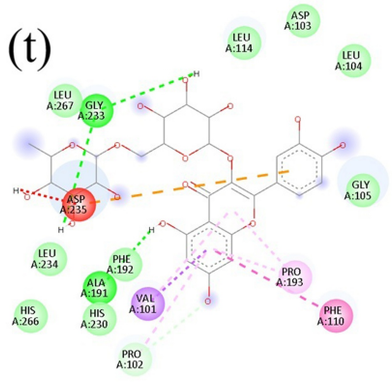
(r)



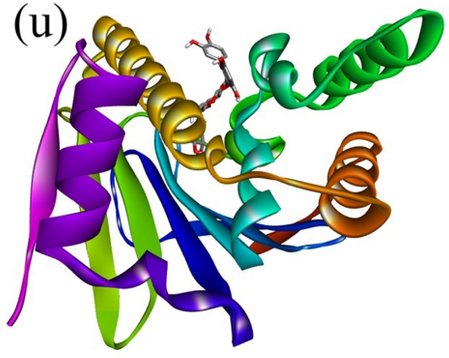
(s)



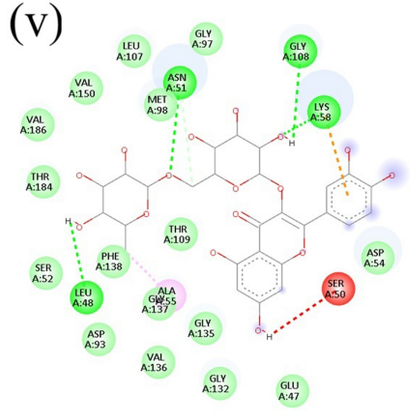
(t)

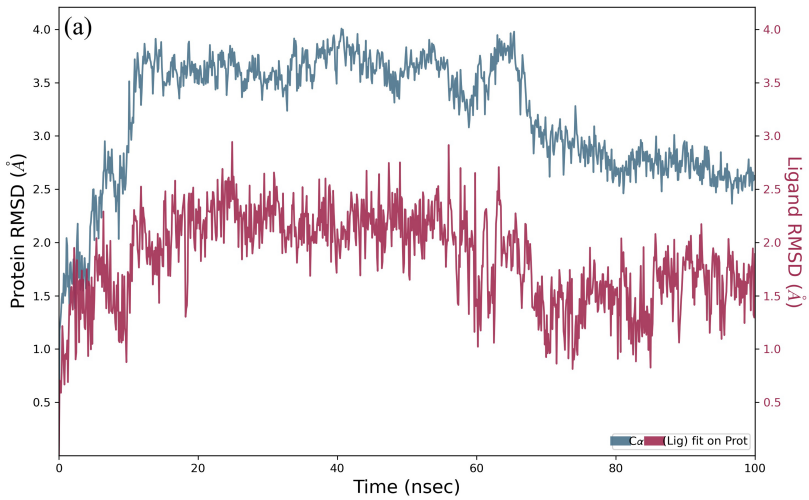


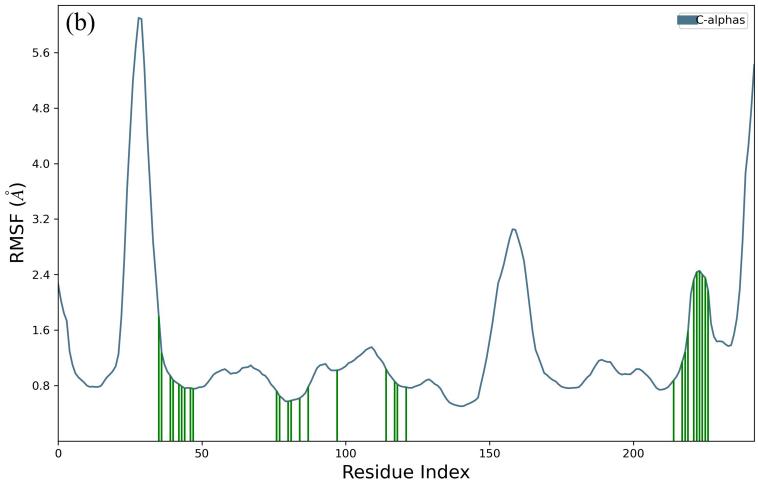
(u)

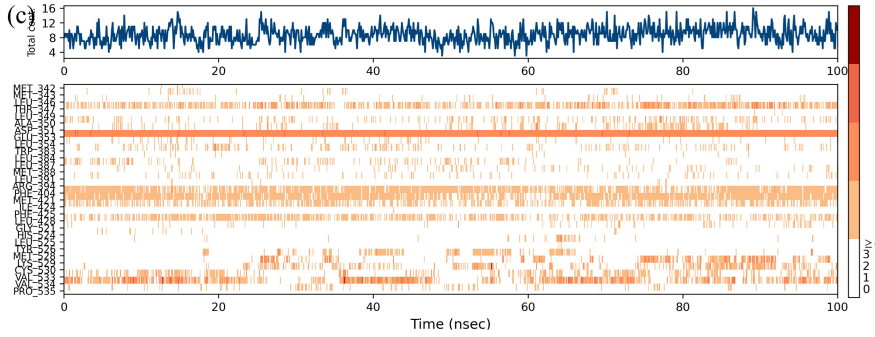


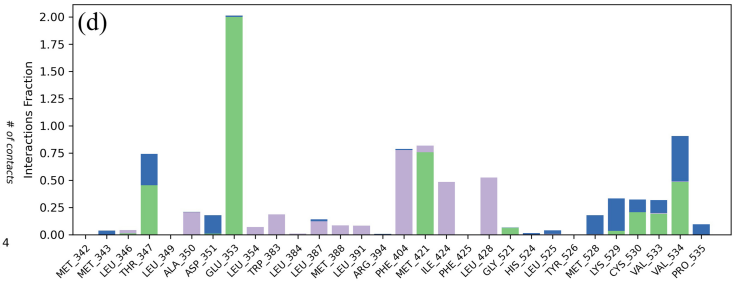
(v)

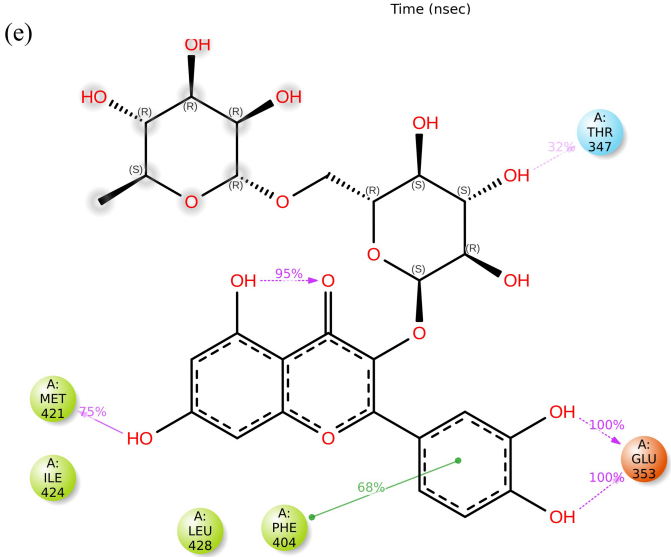


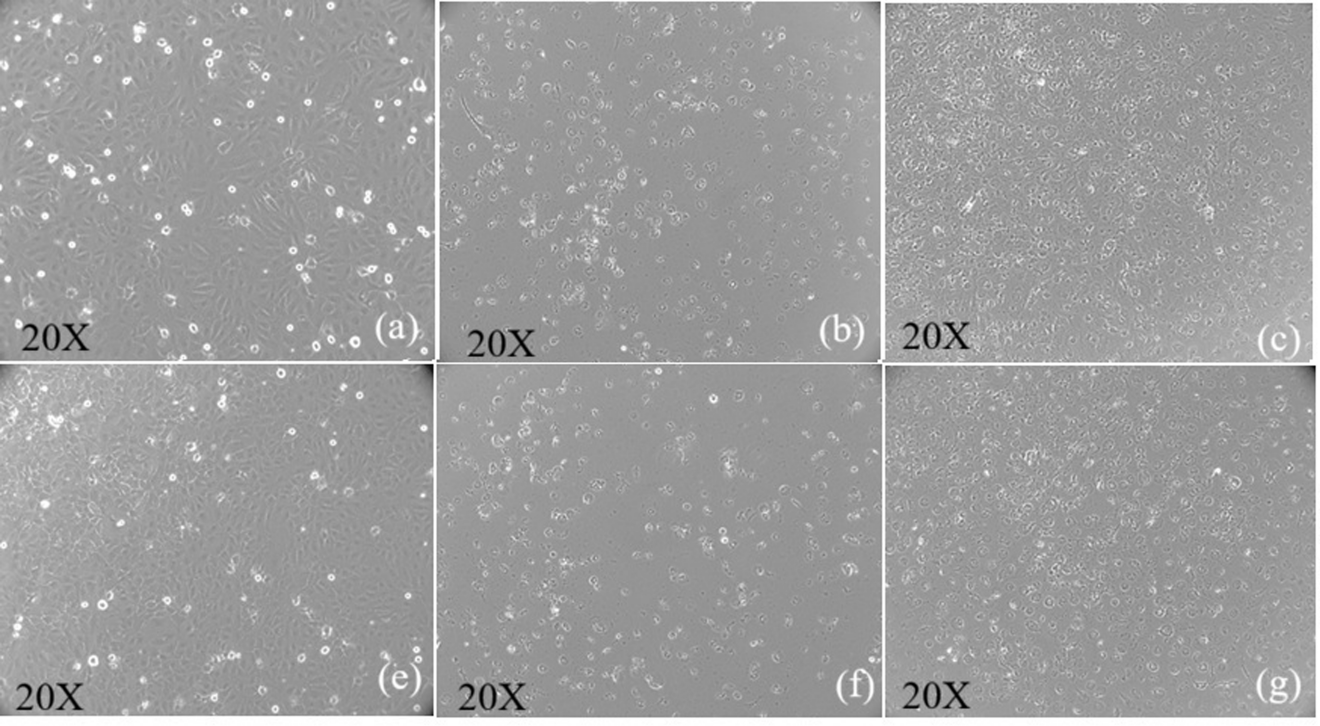

(a)
Protein RMSD (Å)
Ligand RMSD (Å)
Time (nsec)
Cα (Lig) fit on Prot

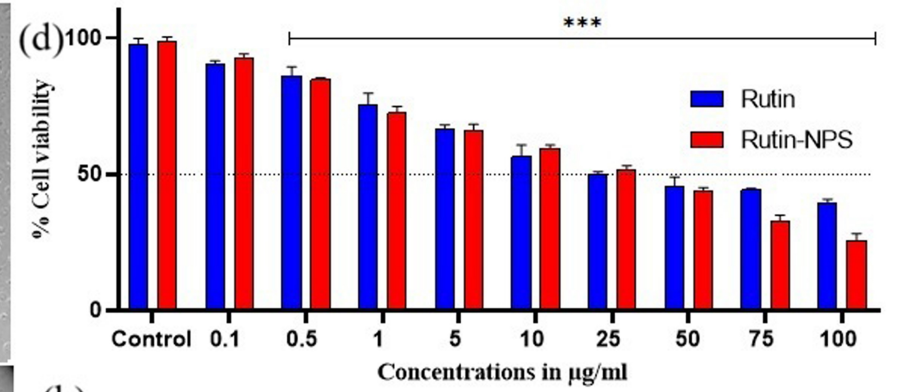

(b)
C-alphas
RMSF (Å)
Residue Index

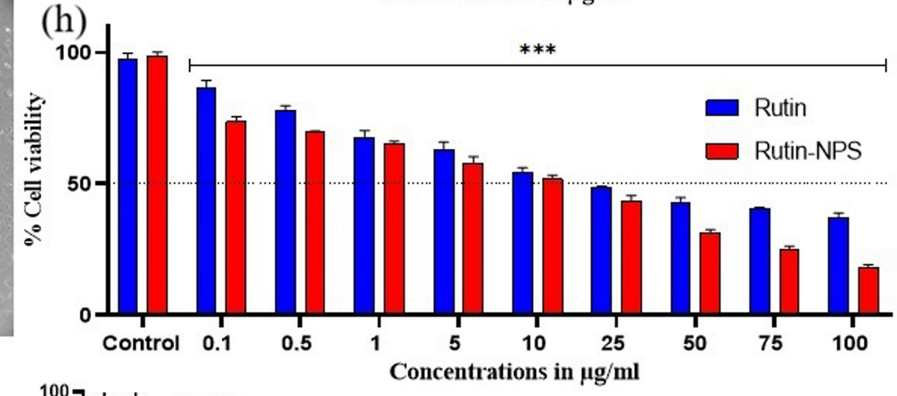

(c)
Total Count
Time (nsec)

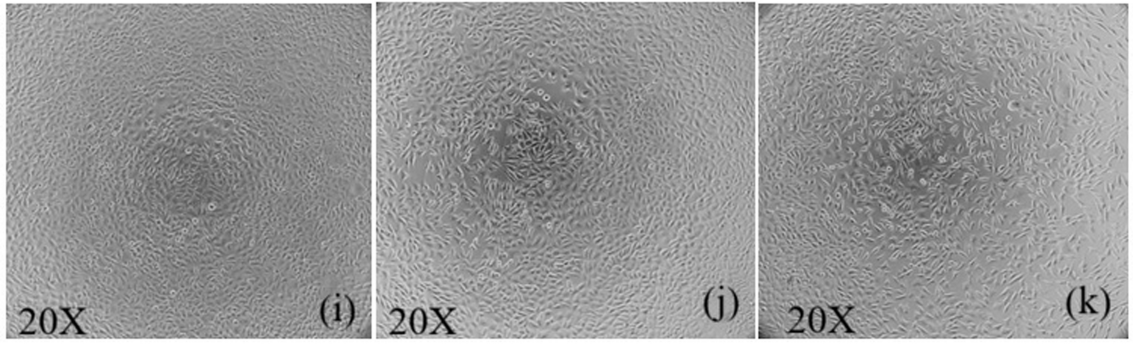

(d)
Interactions Fraction
# of contacts
MET_342
MET_343
LEU_346
THR_347
LEU_349
ALA_350
ASP_351
GLU_353
LEU_354
TRP_383
LEU_384
LEU_387
MET_388
LEU_391
ARG_394
PHE_404
MET_421
ILE_424
PHE_425
LEU_428
GLY_521
HIS_524
LEU_525
TYR_526
MET_528
LYS_529
CYS_530
VAL_533
VAL_534
PRO_535

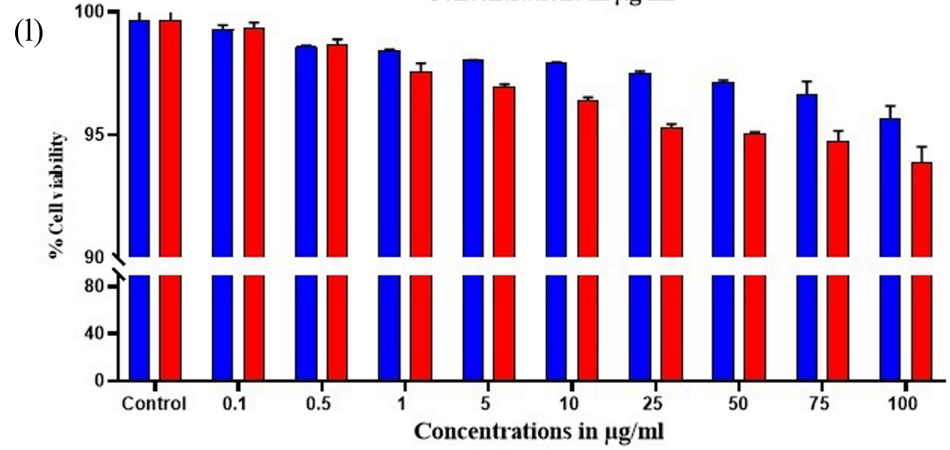

(e)
A: THR 347
A: MET 421
A: ILE 424
A: LEU 428
A: PHE 404
A: GLU 353
32%
95%
75%
68%
100%
100%

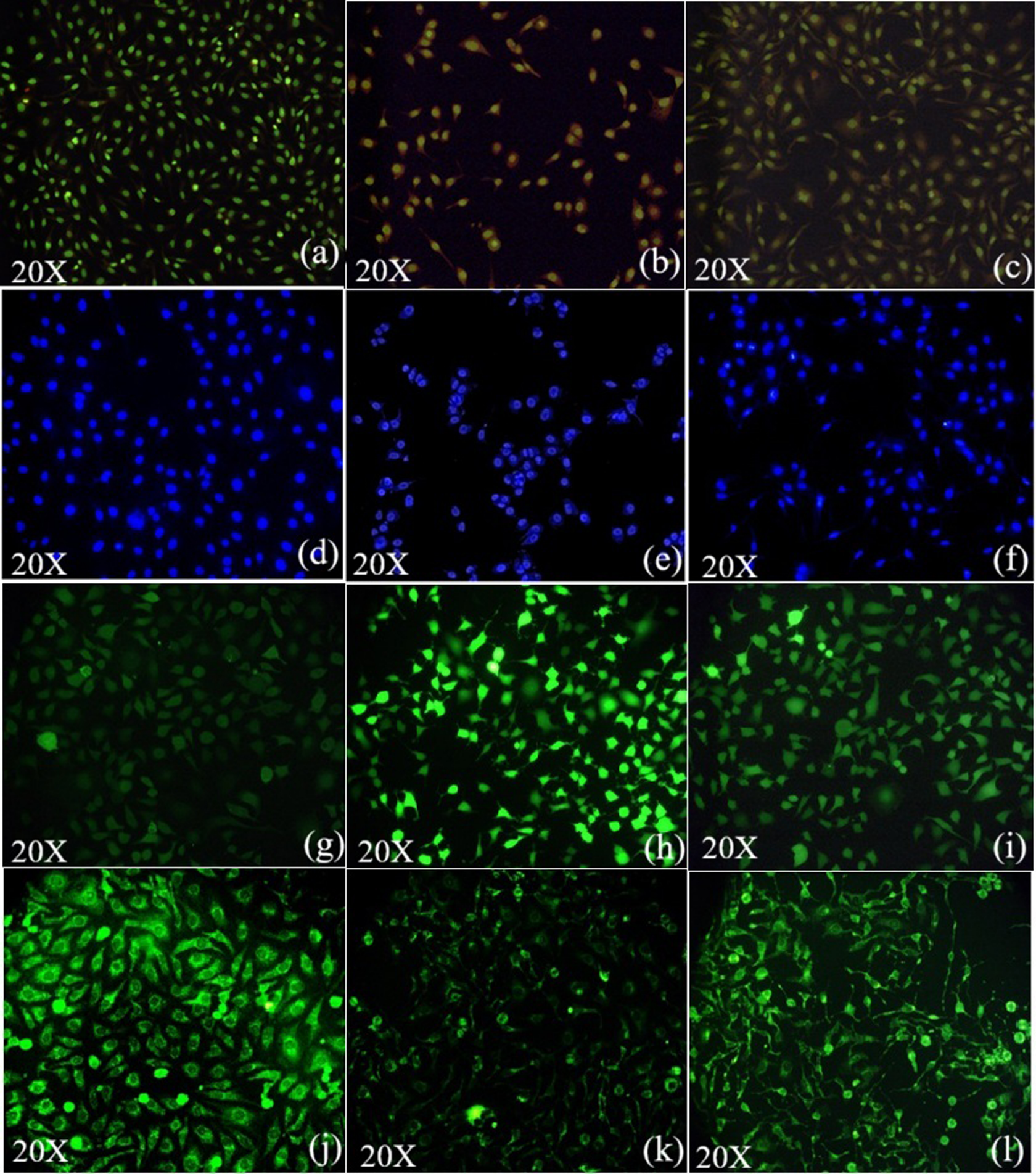

20X
(a)
20X
(b)
20X
(c)
20X
(e)
20X
(f)
20X
(g)

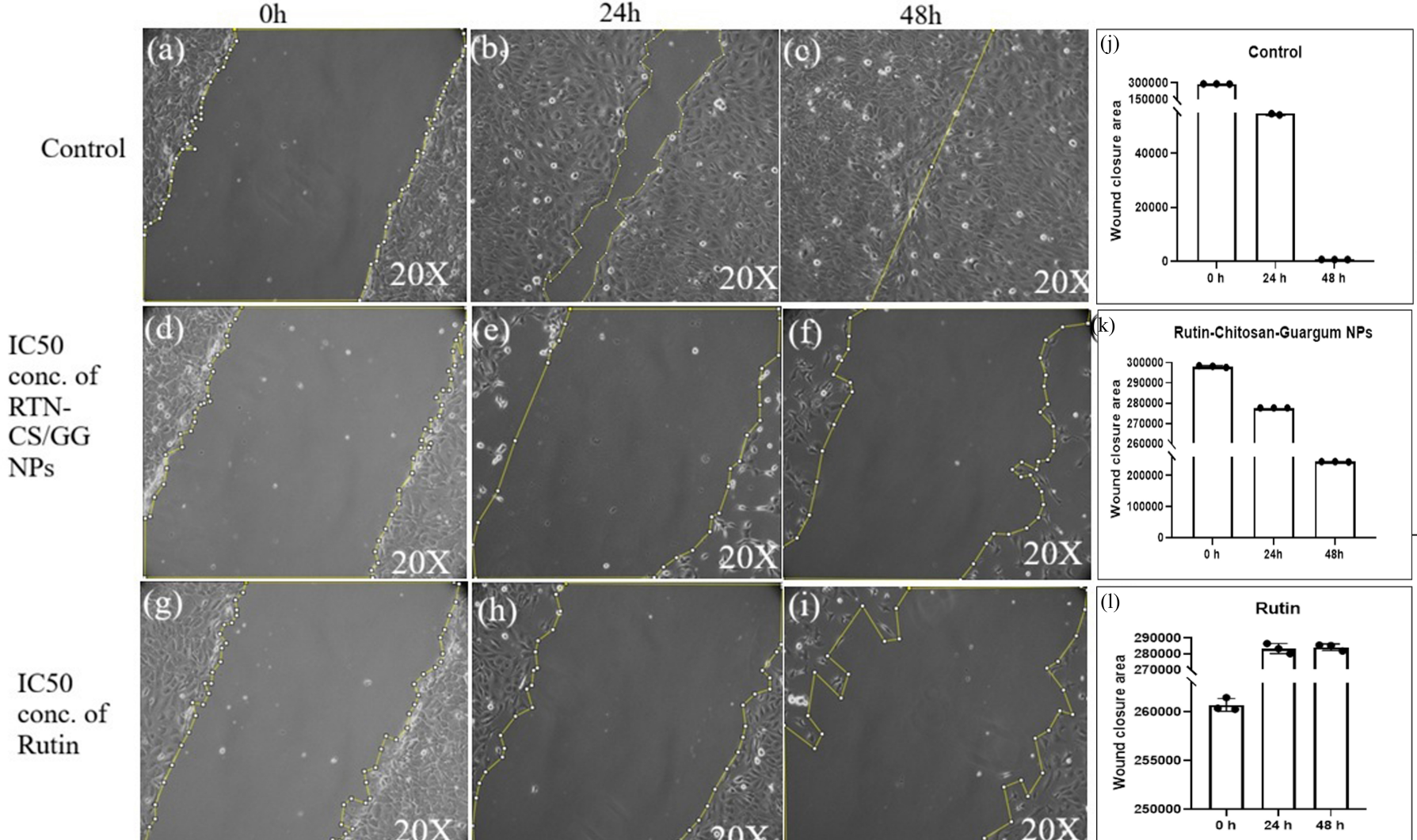

(d)
***
% Cell viability
100
50
0
Rutin
Rutin-NPS
Control
0.1
0.5
1
5
10
25
50
75
100
Concentrations in µg/ml


(h)
***
% Cell viability
100
50
0
Rutin
Rutin-NPS
Control
0.1
0.5
1
5
10
25
50
75
100
Concentrations in µg/ml


20X
(i)
20X
(j)
20X
(k)


(l)
% Cell viability
100
95
90
80
40
0
Control
0.1
0.5
1
5
10
25
50
75
100
Concentrations in µg/ml


20X
(a)
20X
(b)
20X
(c)
20X
(d)
20X
(e)
20X
(f)
20X
(g)
20X
(h)
20X
(i)
20X
(j)
20X
(k)
20X
(l)


0h
24h
48h
Control
IC50 conc. of RTN-CS/GG NPs
IC50 conc. of Rutin
(a)
(b)
(c)
(d)
(e)
(f)
(g)
(h)
(i)
20X
(j)
Control
Wound closure area
300000
150000
40000
20000
0
0 h
24 h
48 h
(k)
Rutin-Chitosan-Guargum NPs
Wound closure area
300000
290000
280000
270000
260000
200000
100000
0
0 h
24h
48h
(l)
Rutin
Wound closure area
290000
280000
270000
260000
255000
250000
0 h
24 h
48 h

Supplementary Files

This is a list of supplementary files associated with this preprint. Click to download.

- Table1.doc
- Table2.doc
- Table3.doc
- supplementaryfile.xlsx